POLITECNICO DI TORINO
Repository ISTITUZIONALE

Enhanced visible-light hydrogen production from lactic acid using Cu-doped TiO2 photocatalysts synthesized via supercritical antisolvent process

Original
Enhanced visible-light hydrogen production from lactic acid using Cu-doped TiO2 photocatalysts synthesized via supercritical antisolvent process / Iannaco, M.C., Iervolino, G., Esposito, S., Muscatello, A., Castellino, M., De Marco, I., Vaiano, V.. - In: INTERNATIONAL JOURNAL OF HYDROGEN ENERGY. - ISSN 0360-3199. - 250:(2026), pp. 1-17. [10.1016/j.ijhydene.2026.155955]

Availability:
This version is available at: 11583/3017203 since: 2026-10-29T21:12:51Z

Publisher:
Elsevier

Published
DOI:10.1016/j.ijhydene.2026.155955

Terms of use:

This article is made available under terms and conditions as specified in the corresponding bibliographic description in the repository

Publisher copyright

(Article begins on next page)

28 November 2026

International Journal of Hydrogen Energy 250 (2026) 155955

Contents lists available at ScienceDirect

International Journal of Hydrogen Energy

journal homepage: www.elsevier.com/locate/he

Enhanced visible-light hydrogen production from lactic acid using Cu-doped TiO_2 photocatalysts synthesized via supercritical antisolvent process

Maria Chiara Iannaco [a], Giuseppina Iervolino [a,*], Serena Esposito [b], Andrea Muscatello [b], Micaela Castellino [b,c,**], Iolanda De Marco [a,***], Vincenzo Vaiano [a]

[a] Department of Industrial Engineering, University of Salerno, Via Giovanni Paolo II, 132, Fisciano, Salerno, 84084, Italy
[b] Department of Applied Science and Technology – Politecnico di Torino, Corso Duca degli Abruzzi 24, Torino, 10129, Italy
[c] Center for Sustainable Future Technologies, Istituto Italiano di Tecnologia, Via Livorno 60, Torino, 10144, Italy

ARTICLE INFO

Keywords:
Cu-doped TiO_2
SAS micronization
Visible-light photocatalysis
Hydrogen evolution
Lactic acid as electron donor

ABSTRACT

Developing highly active TiO_2-based photocatalysts capable of operating under visible light remains a key challenge for scalable solar-to-hydrogen conversion. In this work, we report a significant performance enhancement achieved by SAS micronization to produce Cu-doped TiO_2 photocatalysts with finely tuned structural and electronic properties. Comprehensive characterization (XRD, Raman, FESEM–EDX, FTIR, UV–vis, PL, SSA and XPS) reveals that SAS processing promotes homogeneous Cu incorporation, lattice distortion along the c-axis, and the generation of oxygen vacancies, collectively enabling band-gap narrowing and improved visible-light absorption. Among the investigated samples, 2Cu–TiO_2 SAS exhibited the highest H_2 production (4040 μmol L^{-1} after 4 h), outperforming both non-micronized analogues and literature benchmarks. Photocatalytic tests combined with D_2O experiments demonstrate that lactic acid serves as the primary hydrogen source. A kinetic model derived from the Langmuir–Hinshelwood framework, incorporating substrate inhibition at high lactic-acid concentrations, accurately reproduces the experimental trends and predicts photocatalytic performance. When normalized to catalyst mass, lactic-acid moles, and irradiation power, the 2Cu–TiO_2 SAS photocatalyst achieves 941 μmol H_2 $gcat^{-1}$ mol_{LA}^{-1} W^{-1}, up to twenty times higher than reference CdS-based systems. The novelty of this work lies in the use of the supercritical antisolvent (SAS) process to achieve improved Cu incorporation into the TiO_2 lattice, enabling enhanced visible-light-driven hydrogen production from lactic acid compared to conventionally prepared materials.This study establishes SAS-micronized Cu–TiO_2 as a highly efficient platform for visible-light-driven hydrogen production.

1. Introduction

The transition toward sustainable energy systems is driving increasing interest in alternative hydrogen production routes capable of reducing reliance on fossil fuels and associated CO_2 emissions [1,2]. Among the emerging strategies, photocatalytic hydrogen generation has gained considerable attention as it allows simultaneous H_2 production and the valorization of organic compounds while operating under mild conditions [3,4].

Titanium dioxide (TiO_2) remains one of the most widely investigated photocatalysts due to its stability, non-toxicity, and low cost [5]. However, its relatively wide bandgap (3.0–3.2 eV) restricts absorption to the UV region, and rapid electron–hole recombination limits overall efficiency. Various modification strategies have been proposed to enhance visible-light activity, including metal and non-metal doping [6,7]. Among transition-metal dopants, copper has emerged as a promising candidate, as Cu^{2+}/Cu^{+} species introduce intra-bandgap states, extend light absorption into the visible region, and act as efficient electron

This article is part of a special issue entitled: EFCHC25 conference (Iulianelli) published in International Journal of Hydrogen Energy.

* Corresponding author.
** Corresponding author. Department of Applied Science and Technology – Politecnico di Torino, Corso Duca degli Abruzzi 24, 10129, Torino, Italy.
*** Corresponding author.
E-mail addresses: giervolino@unisa.it (G. Iervolino), micaela.castellino@polito.it (M. Castellino), idemarco@unisa.it (I. De Marco).

https://doi.org/10.1016/j.ijhydene.2026.155955
Received 11 March 2026; Received in revised form 6 May 2026; Accepted 6 June 2026
Available online 16 June 2026
0360-3199/© 2026 The Author(s). Published by Elsevier Ltd on behalf of Hydrogen Energy Publications LLC. This is an open access article under the CC BY license (http://creativecommons.org/licenses/by/4.0/).

traps, thereby improving charge separation [8]. Several studies have demonstrated that Cu-doped TiO_2 can outperform pristine TiO_2 in photocatalytic reactions such as pollutant degradation, CO_2 reduction, and hydrogen evolution [9,10]. Nevertheless, reported performances vary considerably due to differences in synthesis method, dopant dispersion, and copper speciation. Most Cu-doped TiO_2 photocatalysts have been produced using conventional techniques such as sol–gel synthesis, hydrothermal treatment, or wet impregnation. While effective, these routes often provide limited control over particle size, morphology, and metal incorporation, and they may lead to residual contaminants that negatively affect photocatalytic performance [11–14]. Therefore, the development of alternative synthesis methods capable of generating highly uniform and pure nanostructured materials is of increasing relevance.

Supercritical antisolvent (SAS) precipitation has recently emerged as a promising approach for producing advanced metal-oxide photocatalysts. Thanks to the unique properties of supercritical CO_2 (such as high diffusivity and negligible surface tension) SAS enables rapid nanoprecipitation, narrow particle-size distributions, and efficient solvent removal [15,16]. However, despite its potential, the use of SAS for the preparation of metal-doped TiO_2, and in particular Cu-doped TiO_2, remains scarcely explored [17,18].

In this context, the present work investigates the synthesis of Cu-doped TiO_2 with different Cu loadings using the SAS process, followed by thermal activation. The resulting materials were thoroughly characterized to evaluate the influence of doping on structural, morphological, and optical properties. Their photocatalytic performance was assessed in the visible-light-driven hydrogen production from aqueous lactic acid solutions, a sacrificial agent of interest due to its low oxidation potential, biodegradability, and relevance in waste valorization [19,20]. In this context, the present work aims to elucidate the role of the supercritical antisolvent (SAS) process in promoting an effective incorporation of Cu into the TiO_2 lattice and its impact on visible-light-driven hydrogen production. The novelty of this study lies in correlating the synthesis route with the structural properties of the photocatalyst and its performance in lactic acid photoreforming, providing insights into structure–activity relationships. By establishing correlations between material features and photocatalytic activity, this study provides new insights into the role of Cu doping and demonstrates the potential of SAS as an effective technique for preparing next-generation visible-light-active photocatalysts for the hydrogen production.

2. Materials and methods

2.1. Materials

Titanium (IV) oxide acetylacetonate ($TiO(acac)_2$) and copper (II) acetate monohydrate (CuAc) were obtained from Sigma-Aldrich. Ethyl alcohol (99.9% purity) and lactic acid (88% purity) were purchased from Carlo Erba Reagenti. Carbon dioxide (99% purity) was supplied by Morlando Group S.r.l. (Naples, Italy).

2.2. Photocatalyst preparation

2.2.1. Supercritical antisolvent (SAS) process

Micronization of the photocatalyst precursors was carried out using the supercritical antisolvent (SAS) technique. Ethanol was selected as the solvent since both $TiO(acac)_2$ and CuAc are readily soluble in it. For the SAS micronization of pure $TiO(acac)_2$, ethanolic solutions with concentrations of 7 mg/mL and 10 mg/mL were prepared. To obtain Cu-doped photocatalysts with 2%Cu/Ti molar percentage of 2%), $TiO(acac)_2$ and CuAc were dissolved together in ethanol at a total concentration of 10 mg/mL.

The Cu nominal loading is expressed as a molar percentage, and it was evaluated through the following equation:

$$\%mol\ Cu = \frac{nCu}{nCu + nTi} \quad \text{Eq.(1)}$$

where nCu and nTi are the moles of CuAc and $TiO(acac)_2$ used in the synthesis, respectively.

During the SAS process, supercritical CO_2 ($scCO_2$) was pumped into a high-pressure precipitation chamber and brought to the desired operating pressure. Once steady-state conditions were reached, pure ethanol was introduced through a high-pressure pump and sprayed through a stainless-steel nozzle. The precursor solution was then injected into the chamber at a flow rate of 1 mL/min. Upon contact with $scCO_2$, rapid mutual diffusion of solvent and antisolvent induced solute supersaturation, leading to homogeneous precipitation of micronized particles.

After precipitation, a washing step with $scCO_2$ was carried out to remove solvent residues. The vessel was then depressurized to atmospheric pressure, and the resulting particles were collected from the filter, characterized, and used for photocatalytic testing.

All SAS experiments were performed at 150 bar and 40 °C, using a 100 μm injector and a CO_2 flow rate of 30 g min^{-1}. A detailed scheme of the SAS apparatus is reported elsewhere [21].

The recovered powder was subjected to a slow calcination treatment, heating at a rate of 2 °C min^{-1} up to 450 °C and maintaining this temperature for 2 h. Throughout this work, the resulting materials are referred to as micronized TiO_2 (TiO_2 SAS) and micronized 2Cu-doped TiO_2.

2.2.2. Solution-based synthesis (evaporation–calcination route)

For comparison purposes, a conventional solution-based method was employed to assess the feasibility of Cu doping in TiO_2 and to benchmark the resulting materials against those prepared via the SAS process. Copper acetate and titanium oxide acetylacetonate were dissolved in ethanol, maintaining a nominal Cu molar percentage of 2%. The solution was stirred at room temperature until complete solvent evaporation was achieved. The resulting solid residue was collected as a dry powder.

The obtained powder was then subjected to calcination, with a heating rate of 2 °C min^{-1} up to 450 °C and a dwell time of 2 h. The following photocatalysts were obtained and tested:

- TiO_2 derived from the non-micronized precursor (TiO_2 NM),
- Cu-doped TiO_2 derived from the non-micronized precursor (2Cu–TiO_2 NM).

2.3. Characterization methods

All precursor samples and the corresponding calcined catalysts were dispersed onto a carbon tray coated with a 250 Å-thick gold layer. The morphology was examined using a field emission scanning electron microscope (FESEM, LEO 1525, Carl Zeiss SMT AG). The average particle diameter and particle size distribution were determined through image analysis performed with Sigma Scan Pro v5.0 (Aspire Software International) and graphically processed using Origin software. Energy-dispersive X-ray (EDX) analysis was also conducted to confirm the presence of copper in the photocatalysts.

X-ray diffraction (XRD) patterns were collected using a Bruker D8 diffractometer equipped with Cu Kα radiation. The lattice parameters were calculated using the following equation:

$$\frac{1}{d^2_{(h\ k\ l)}} = \frac{h^2 + k^2}{a^2} + \frac{l^2}{c^2} \quad \text{Eq.(2)}$$

In these equations, h, k, and l are the Miller indices; $d_{(h\ k\ l)}$ is the interplanar distance; and a, and c are the lattice parameters (for tetragonal anatase TiO_2 $a = b \neq c$). The anatase (1 0 1) and (2 0 0) diffraction planes were used to determine the lattice parameters [22].

The average crystallite size was estimated using the Scherrer equation [23].

Infrared spectra were collected using a Fourier-transform infrared (FT-IR) Alpha spectrometer (Bruker Optics). A total of 100 mg of KBr was mixed with 1 mg of the sample to form an IR-transparent pellet. Spectra were recorded in the wavenumber range of 4000–400 cm^{-1}.

Raman spectra were acquired at room temperature using a dispersive Raman micro-spectrometer (Renishaw, India) equipped with a 514 nm excitation laser. Measurements were performed in the Raman shift range of 200–2000 cm^{-1}.

UV–Vis diffuse reflectance (UV–Vis DRS) spectra were obtained using a PerkinElmer Lambda 35 spectrometer equipped with an RSA-PE-20 reflectance accessory (Labsphere Inc.). Measurements were carried out using an 8° sample holder, and total reflectance was referenced to a calibrated SRS-010-99 standard. The optical bandgap was evaluated using the Kubelka–Munk function, F(R), by plotting $[F(R)\times h\nu]^{1/2}$ as a function of photon energy $h\nu$ (eV).

X-ray photoelectron spectroscopy (XPS) measurements were performed using a PHI 5000 VersaProbe II spectrometer equipped with a monochromatic Al Kα X-ray source. Charge compensation was achieved using a dual system combining low-energy electrons and Ar^+ ions. The conditions used for all survey scans were as follows: energy range 1200–0 eV, pass energy 187.85 eV, step size 0.8 eV, step time 20 ms, and X-ray spot size 100 μm. For high-resolution (HR) spectra, an energy range 50–20 eV was used, with a pass energy of 23.50 eV and a step size of 0.1 eV, step time 50 ms, and X-ray spot size 100 μm. The binding energy scale was referenced to the C–C peak of C1 at 284.8 eV, attributed to the adventitious carbon. All spectra were analyzed using CasaXPS version 2.3.18 software. The background of each spectrum was subtracted using a Shirley function. Relative atomic concentration values were deduced from the HR spectra to get more reliable values than from survey spectra.

A PerkinElmer Spectrofluorometer LS55 was used to record the fluorescence spectra. The emission spectrum was acquired using an excitation wavelength (λ_{ex}) of 365 nm, with both excitation and emission slits set to 10 nm, and employing a 390 nm cut-off filter to suppress scattered excitation light. Textural characterization was performed via N_2 physisorption and desorption isotherms at −196 °C, utilizing a Micromeritics ASAP 2020 instrument. Prior to analysis, samples underwent an outgassing procedure at 250 °C for 3 h under high vacuum to eliminate residual contaminants. The specific surface area (SSA) was derived using the Brunauer–Emmett–Teller (BET) model, while the pore size distribution was determined from the desorption branch via the Barrett–Joyner–Halenda (BJH) method.

The optimal photocatalyst was used to investigate the effect of lactic acid concentration on the average aggregate size and Z-potential of the catalyst suspension. Measurements were performed by Dynamic Light Scattering (DLS) using a Malvern Zetasizer Nano S (Malvern Instruments). The aggregate size was expressed as Z-average diameter, while Z-potential measurements were used to evaluate the colloidal stability of the suspension as a function of lactic acid concentration (0-40 vol%).

2.4. Photocatalytic activity tests

Photocatalytic hydrogen production tests were carried out using a dedicated experimental setup. A cylindrical Pyrex batch reactor (inner diameter: 2.5 cm; height: 18 cm), equipped with a nitrogen distribution system controlled by a mass flow controller (N_2 flow rate: 0.250 NL min^{-1}), was employed. Nitrogen was used both to purge the reactor and to transport the evolved gaseous products to the analyzer, while also contributing to the mixing of the suspension.

A 16 vol% aqueous lactic acid solution (pH = 2.1) was used as the reaction medium, with a total volume of 60 mL. Catalyst loadings in the range of 0.5–2 g L^{-1} were tested. Continuous mixing of the suspension was ensured by a Watson–Marlow peristaltic pump, which provided steady recirculation of the liquid phase through the reactor. Before illumination, the system was left under dark conditions for 60 min.

Photocatalytic reactions were then conducted under visible-light irradiation (λ = 400–600 nm) for up to 240 min. Illumination was provided by four Philips lamps (8 W each) positioned symmetrically around the reactor to ensure uniform irradiation of the suspension. The emission spectrum of the lamps is confined within the visible region; therefore, no additional cutoff filter was required. Although the light intensity was not directly measured, the experimental setup was kept constant for all tests to ensure reliable comparison among the investigated photocatalysts.

The evolved gases were quantified using a gas analyzer (ABB, Advance Optima AO2000) equipped with a CALDOS thermal conductivity module for H_2 detection and a URAS non-dispersive infrared (NDIR) module for CO_2 analysis, connected to LabVIEW software for real-time acquisition of the H_2 and CO_2 concentrations in the outlet stream. The collected data were subsequently processed using Origin software. A schematic diagram of the experimental setup is provided in our previous work [24].

Table S1 of the Supplementary Materials summarizes the main operating conditions of the photocatalytic experiments performed. Specifically, tests were conducted on undoped TiO_2 prepared using non-micronized and SAS-micronized precursors to evaluate the effect of the micronization process on photocatalytic performance. Subsequently, the Cu–TiO_2 catalysts obtained by the SAS process and sol-gel method were tested to assess the effective doping of the photocatalyst. Once the catalyst with the best photocatalytic performance was identified, the effects of catalyst dosage and lactic acid concentration on the photocatalytic hydrogen production were investigated.

3. Results and discussion

3.1. SAS micronization of TiO(acac)$_2$

While methanol is traditionally used as the solvent for processing TiO(acac)$_2$ via the SAS method [25,26], in this study, ethanol was selected as a safer and more sustainable alternative. As previously described, TiO(acac)$_2$ was dissolved in ethanol and processed at 40 °C and 150 bar. The effect of precursor concentration was assessed by preparing solutions at 7 mg mL^{-1} and 10 mg mL^{-1}. After SAS processing, the micronized powders were collected from the precipitator and subjected to physicochemical characterization. The FESEM image of the unprocessed precursor (Fig. S1a), reported in the Supplementary Materials, shows the presence of large aggregates, whereas the SAS-processed precursor precipitated as nanometric particles, as clearly observed in Fig. S1b–c. Solution concentration plays a key role in the SAS precipitation mechanism. The position of the operating point relative to the critical point of the CO_2–organic solvent mixture strongly influences particle formation [27]. However, since nanometric particles were successfully produced at both concentrations tested, it can be inferred that the concentration range explored here does not significantly alter the phase behavior of the CO_2–ethanol mixture, indicating that the system operates above the mixture's critical point. Under such conditions, the gas-mixing precipitation mechanism becomes dominant: solids nucleate and grow directly from the liquid solution, which undergoes instantaneous mixing with the supercritical phase [21,28]. The non-spherical morphology of the nanoparticles further supports this mechanism, as particle formation via droplet drying would typically result in nearly spherical particles due to surface tension effects. Despite operating above the mixture critical point, solute concentration still significantly influences the final particle size, as it directly affects nucleation and growth rates. At the lower concentration (7 mg mL^{-1}), the SAS-processed material tends to form aggregates and exhibits limited particle separation (Fig. S1b). In contrast, the higher concentration (10 mg mL^{-1}) leads to well-defined nanoparticles with an average diameter of 39.3 ± 1.21 nm, as shown by the particle size distribution in Fig. S1d. Generally, increasing the initial solute concentration produces two opposing effects: (i) higher supersaturation promotes rapid nucleation, reducing the available

growth time and limiting particle enlargement before new nuclei form [29]; (ii) higher solute content also enhances condensation rates, favoring particle growth [30]. Under the operating conditions considered in this study, the first effect dominates, resulting in smaller and more uniform particles at higher precursor concentration. Fig. S2 of Supplementary Materials reports the FESEM images of the samples prepared in the presence of copper. The incorporation of copper acetate did not induce appreciable changes in particle morphology compared to the corresponding undoped materials, both for the sol–gel samples and for those obtained via SAS micronization. The SAS-produced particles (Fig. S2b) preserved their spherical shape with no noticeable agglomeration or structural defect attributable to copper addition. These results indicate that, at the investigated copper loading, the metal precursor does not significantly perturb the nucleation-growth mechanism of the process, allowing copper incorporation without compromising the structural integrity of the material.

3.2. Photocatalysts characterization results

FESEM analyses were also carried out to evaluate the morphology of the samples after the calcination step. As shown in Fig. 1, the nanoparticle-like morphology is preserved following thermal treatment, which can be attributed to the use of a slow heating rate during calcination. Fig. 1c–d shows that SAS-produced samples maintain their overall shape, and no significant sintering or extensive grain coalescence are observed. The preservation of the nanoscale structure is particularly important, as it ensures that the high surface area and reactivity associated with the as-prepared materials are largely retained after heat treatment.

Additionally, representative EDX images of Cu-combined TiO_2 samples were acquired to assess their elemental composition, as illustrated in Fig. 2. The analyses confirm the presence of Ti, O, and Cu in both the sol–gel–prepared photocatalyst and the catalyst derived from the SAS-micronized precursors.

A closer examination of the EDX elemental maps for the SAS-derived sample (Fig. 2b) reveals that Cu is finely and uniformly distributed across the TiO_2 matrix, with no evidence of dopant-rich agglomerates. This demonstrates the efficiency of the SAS process in ensuring intimate mixing between Ti and Cu precursors during nanoparticle formation.

In contrast, the non-SAS sample (2Cu–TiO_2 NM, Fig. 2a) shows a noticeably less uniform distribution of copper. The EDX maps reveal localized areas of Cu enrichment and a more heterogeneous dopant distribution, evidencing the formation of Cu-rich domains.

Fig. 3a shows the XRD patterns of the non-micronized photocatalyst, the SAS-micronized photocatalyst, and the Cu-combined samples.

All materials exhibit the characteristic diffraction peaks of the tetragonal anatase TiO_2 phase (JCPDS 21-1272). All samples, both doped and undoped, display the characteristic diffraction peaks at $2\theta = 25.3^\circ$ corresponding to the (101) plane and at $2\theta \approx 48^\circ$ corresponding to the (200) plane of the anatase TiO_2 structure.

As shown in Fig. 3b, the 2Cu–TiO_2 SAS photocatalyst exhibits a slight shift of the (101) diffraction peak from $2\theta \approx 25.3^\circ$ toward lower 2θ values. This shift is indicative of lattice expansion, which can be attributed to the incorporation of Cu species into the TiO_2 lattice,

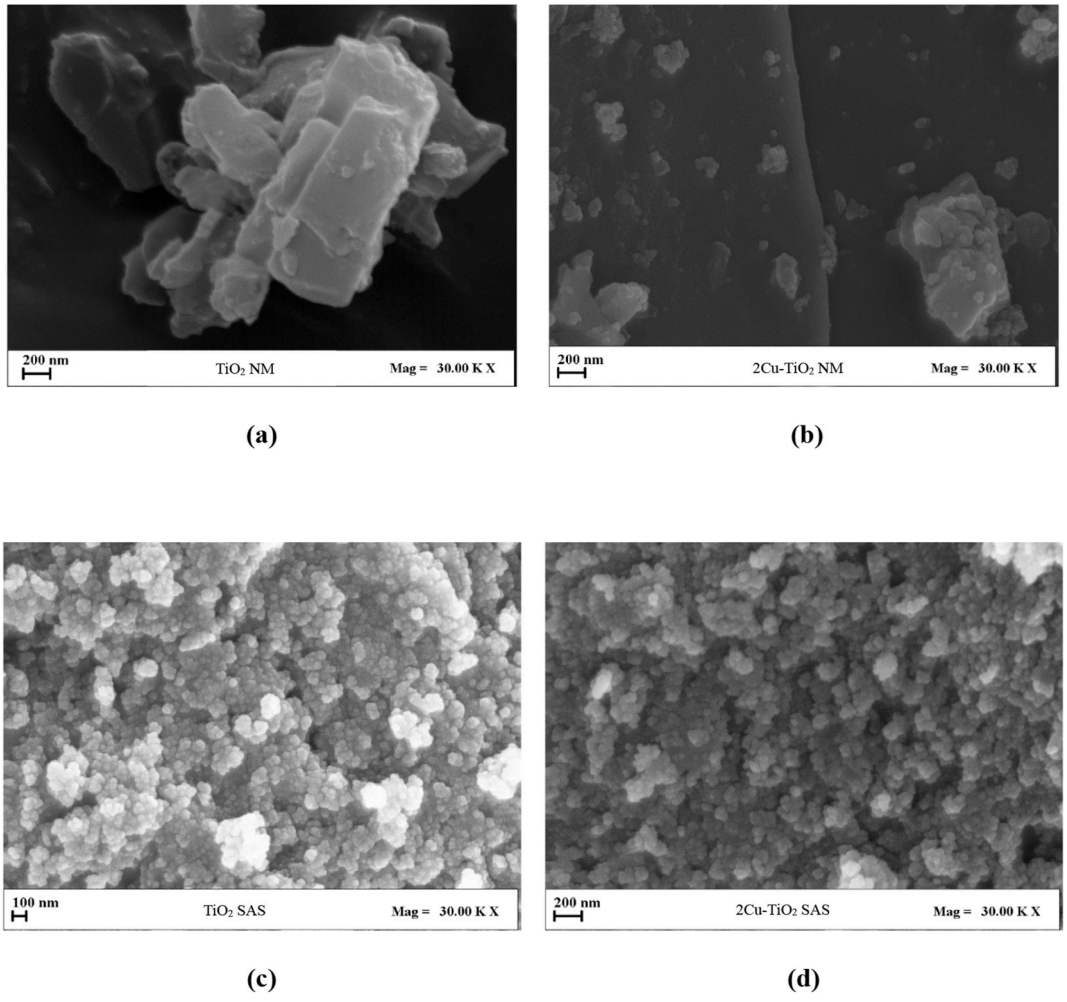

Fig. 1. FESEM images of (a) TiO_2 NM, (b) 2Cu–TiO_2 NM, (c) TiO_2 SAS, (d) 2Cu–TiO_2 SAS.

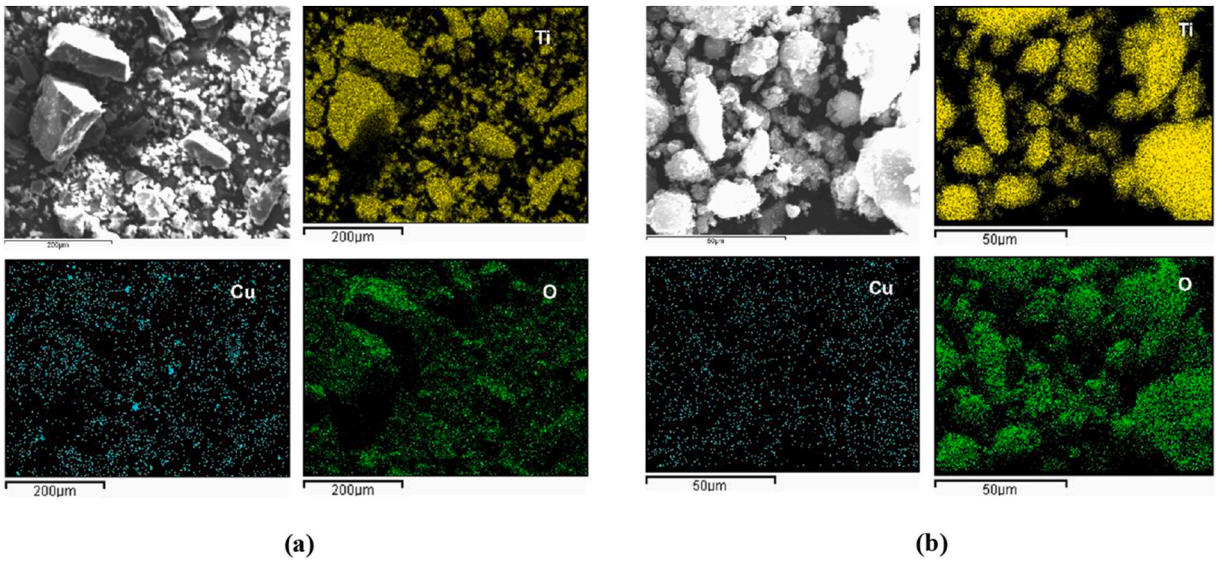

Fig. 2. EDX images of (a) 2Cu–TiO_2 NM, (b) 2Cu–TiO_2 SAS.

producing local structural distortion due to the ionic radius mismatch between Cu^{2+} (0.73 Å) and Ti^{4+} (0.64 Å) [31]. Importantly, this shift is not observed in the 2Cu–TiO_2 NM sample, suggesting that the sol–gel synthesis route does not effectively facilitate the incorporation of Cu species into the TiO_2 lattice structure.

2Cu–TiO_2 SAS sample shows an additional weak diffraction peak at $2\theta \approx 34.9°$, attributable to Ti_2O_3 [32]. Additionally, the slight broadening of the main anatase reflection at $2\theta \approx 25°$ can be reasonably attributed to the partial overlap with a weak reflection at $2\theta \approx 24.9°$ of rhombohedral-phase Ti_2O_3 (JCPDS 43-1033). Their very low intensity indicates that the Ti_2O_3 phase is present only in trace amounts; in fact, Raman and UV-Vis spectroscopies (*vide infra*) do not reveal discernible features attributable to Ti_2O_3, confirming that this phase constitutes a minor impurity and does not significantly affect the crystal structure of the dominant TiO_2 matrix.

Furthermore, the lack of the characteristic CuO diffraction peaks attributable to CuO or Cu_2O suggests that copper does not crystallize as a separate oxide phase [33].

Given the results discussed above, it is reasonable to conclude that the SAS-micronized sample undergoes an effective Cu incorporation within the TiO_2 lattice, consistent with a doping process.

This conclusion is further supported by the lattice parameter values reported in Table 1. Compared to pure TiO_2 SAS, the 2Cu–TiO_2 SAS sample exhibits a measurable increase in the *c* lattice parameter, while the *a* parameter remains essentially unchanged within experimental uncertainty. This anisotropic lattice expansion is consistent with the incorporation of Cu species into the TiO_2 lattice and with the formation of charge-compensating oxygen vacancies, both of which can contribute to a slight elongation of the unit cell along the *c* axis [34]. In contrast, the lattice parameters of the 2Cu–TiO_2 NM sample remain very similar to those of the undoped TiO_2, indicating that the sol–gel synthesis route does not effectively promote the incorporation of Cu species into the TiO_2 lattice.

Furthermore, the crystallite size values calculated using the Scherrer equation (Table 1) reveal no significant differences among the investigated samples. Both undoped and Cu-doped photocatalysts (irrespective of whether they were synthesized via SAS or prepared from the non-micronized precursor) exhibit comparable crystallite sizes. This demonstrates that neither the introduction of copper nor the different synthesis methods substantially affects the growth of anatase nanocrystallites during calcination. The structural modifications observed in Cu-doped SAS samples therefore arise primarily from lattice distortions associated with dopant incorporation rather than from variations in crystallite size.

Fig. 4 reports the FTIR spectra of all photocatalysts investigated. All samples display a broad absorption band in the 1000–400 cm^{-1} region, attributable to Ti–O stretching vibrations (≈490 cm^{-1}) and Ti–O–Ti bridging modes (≈730 cm^{-1}), which are characteristic of anatase titania [35].

The band at 1636 cm^{-1} corresponds to Ti–OH bending vibrations arising from molecular water adsorbed on the TiO_2 surface [36]. The feature observed around 2340 cm^{-1} is associated with the asymmetric stretching of CO_2, typically resulting from the interaction between atmospheric CO_2 and surface hydroxyls [37]. The broad band centered at approximately 3440 cm^{-1} is assigned to the symmetric and asymmetric stretching vibrations of surface hydroxyl groups (Ti–OH) [38].

When copper is introduced into TiO_2, an increase in surface hydroxylation can be inferred by comparing the relative intensity of the broad O–H stretching band at approximately 3440 cm^{-1} with that of the Ti–O–Ti bridging vibration at ~730 cm^{-1}. In particular, the ratio between the 3440 cm^{-1} and 730 cm^{-1} bands increases upon Cu addition, with the effect being most evident for the 2Cu–TiO_2 SAS sample. A plausible explanation is the formation of oxygen vacancies associated with the incorporation of Cu^{2+} into the TiO_2 lattice [39]. Oxygen vacancies act as active sites for water adsorption, resulting in the formation of surface –OH groups and enhancing the hydrophilicity of the material. Moreover, a higher concentration of hydroxyl groups can promote the adsorption of lactic acid onto TiO_2 through acid deprotonation and hydrogen bonding interactions [40].

To support the assessment of oxygen vacancies, Raman spectra of the bare and Cu-doped samples were recorded in the 100–800 cm^{-1} region. Fig. 5reports the Raman spectra of all investigated photocatalysts. The typical Raman-active modes of anatase TiO_2 are clearly observed at 144 (E_g), 195 (E_g), 394 (B_{1g}), 516 ($A_{1g} + B_{1g}$), 639 cm^{-1} (E_g), confirming the formation of the anatase phase in all samples [41,42].

The E_g mode at ~144 cm^{-1} is the most intense and sensitive Raman feature of anatase, and its position is known to shift in response to structural disorder, dopant incorporation, or defect formation. Although particle-size effects (phonon confinement) may also influence this peak [43], this mechanism can be excluded here because all investigated samples exhibit comparable crystallite sizes, as demonstrated by Scherrer analysis (Table 1). Therefore, the variations observed in the E_g Raman mode must arise from changes in the crystal lattice rather than from differences in particle size.

The magnified view in Fig. 5a highlights a blue shift of the E_g band in the SAS-derived Cu-doped sample. This behavior is consistent with

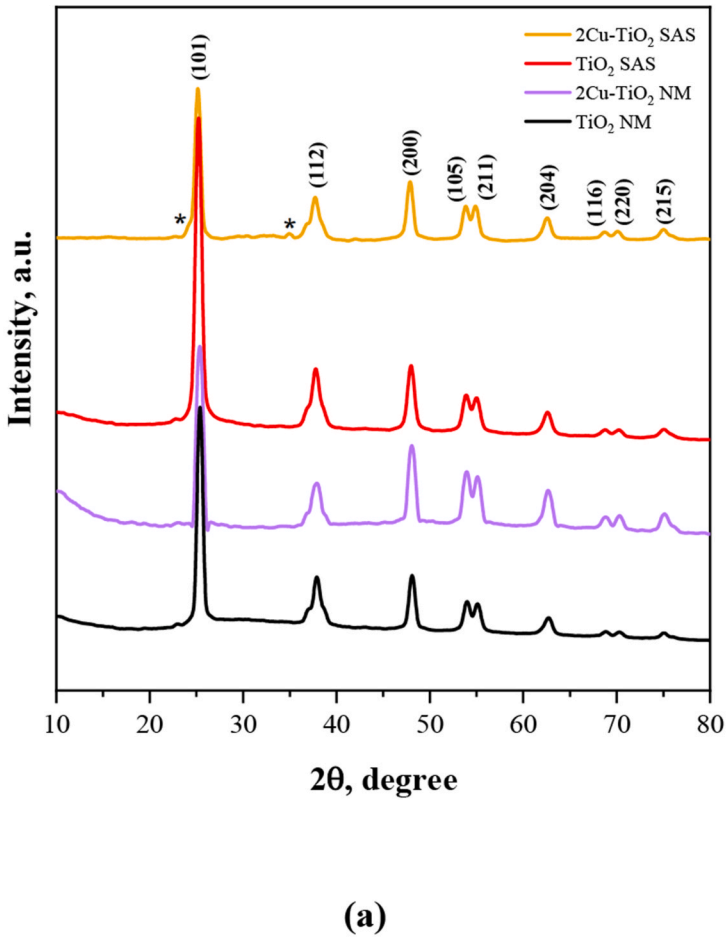

(a)

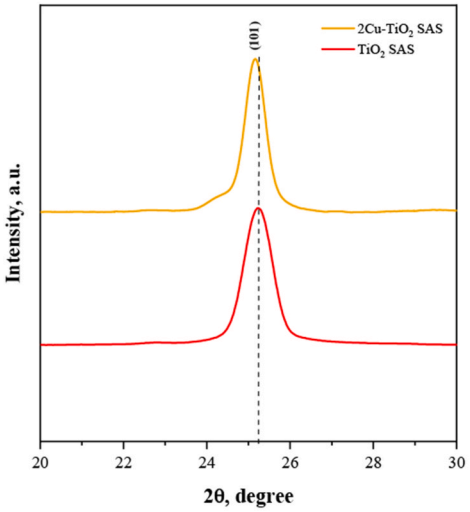

(b)

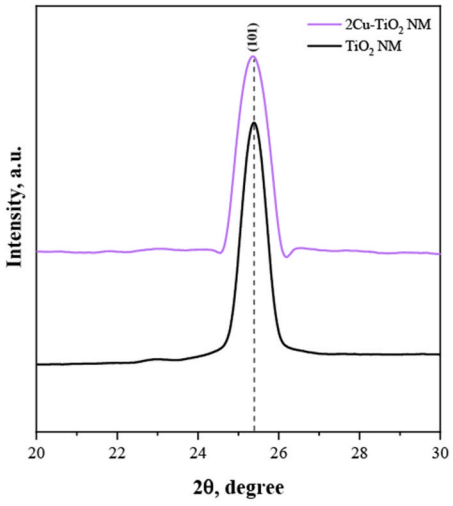

(c)

Fig. 3. (a) XRD patterns of TiO_2 SAS, TiO_2 NM, 2Cu–TiO_2 SAS, and 2Cu–TiO_2 NM samples acquired in the 2θ range of 20–70°. (b) Magnified view of the anatase (101) diffraction peak for TiO_2 SAS and 2Cu–TiO_2 SAS in the 2θ range of 20–30°. (c) Magnified view of the anatase (101) diffraction peak for TiO_2 NM and 2Cu–TiO_2 NM in the 2θ range of 20–30°.

Table 1
Crystallite size and lattice parameter of TiO_2 NM, TiO_2 SAS, 2Cu–TiO_2 NM, and 2Cu–TiO_2 SAS.

Photocatalyst	Crystallite size, nm	Lattice parameter, Å	
		a = b	c
TiO_2 NM	11	3.781	9.339
TiO_2 SAS	10	3.796	9.618
2Cu–TiO_2 NM	11	3.781	9.339
2Cu–TiO_2 SAS	11	3.797	9.937

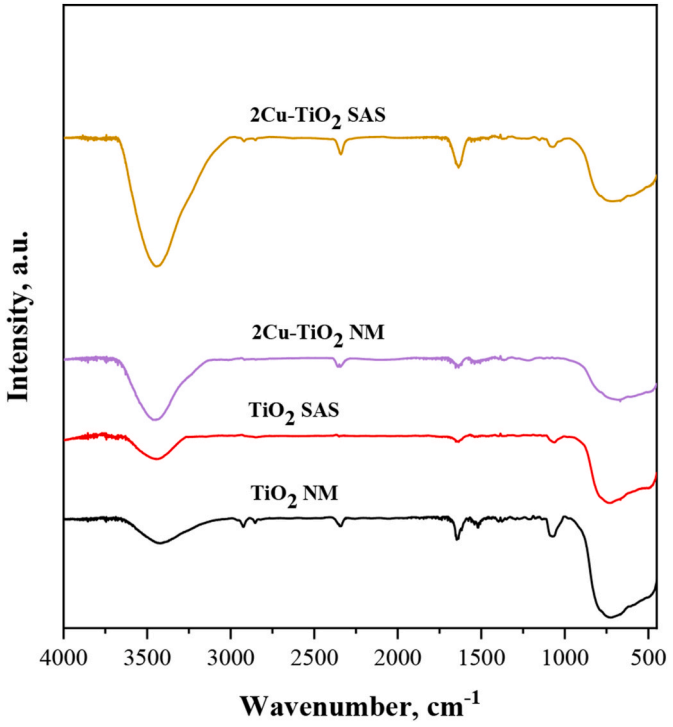

Fig. 4. FT-IR spectra of TiO_2 NM, TiO_2 SAS, 2Cu–TiO_2 NM, and 2Cu–TiO_2 SAS in the 4000–400 cm^{-1} range.

increased lattice distortion, which can originate from the incorporation of Cu species into the TiO_2 lattice and from the generation of oxygen vacancies required for charge compensation [44]. Both phenomena alter the local bonding environment, breaking some of the original Ti–O–Ti linkages and creating Cu–O–Ti or Cu–O–Cu bonds, thereby perturbing the symmetric O–Ti–O stretching mode responsible for the E_g band. Theoretical studies further support that oxygen vacancies in Cu-doped TiO_2 induce a blue shift of the E_g mode [45–47]. In sharp contrast, the non-micronized samples (Fig. 5b) do not exhibit any blue shift of the E_g mode upon Cu addition. This observation corroborates the XRD and lattice-parameter results, which show that Cu is not effectively incorporated into the TiO_2 lattice in the 2Cu–TiO_2 NM sample, where the unit-cell parameters remain almost identical to those of pure TiO_2.

Finally, Cu-combined samples exhibit lower Raman intensities compared to their undoped counterparts. A reduction of Raman signal intensity is commonly reported in Cu-doped TiO_2 systems and can arise from dopant incorporation [48,49]. In addition to this effect, the formation of segregated, as evidenced in the UV-Vis DRS results for 2Cu–TiO_2 NM (*vide infra*), can further attenuate the Raman intensity of anatase, as CuO can act as an absorbing or scattering phase that decreases the effective Raman scattering volume of TiO_2 [50,51].

XPS characterization was conducted to determine the surface chemical composition of the following samples: 2Cu–TiO_2 NM, 2Cu–TiO_2 SAS, TiO_2 NM and TiO_2 SAS. The XPS survey spectra (see Fig. 6) of the samples confirm the presence of Ti, O, and Cu as the main elements, with no detectable impurities above the instrumental detection limit. The Ti and O contributions correspond to the TiO_2 support, whereas Cu is observed consistently across the series, with relative intensities increasing in sample prepared via the NM method. The absence of additional signals (e.g., C 1s only showing adventitious carbon) indicates that the synthesis procedure does not introduce foreign elements. All the relative atomic concentrations values are reported in Table 2. After high resolutions (HR) spectra peak fitting (see Fig. 7), for the C 1s and O 1s regions, the amount of oxygen detected in all the samples has been divided between the components due to direct bonds within the adventitious carbon contamination and the oxides present on the samples surface. It is worth mentioning that sample 2Cu–TiO_2 NM exhibits the highest amount of C (36.1 at.%) and oxygen bonded with it (16.1 at.%), together with Cu content (0.7 at.%). High-resolution spectra of the Cu 2p3/2 – Cu 2p1/2 regions (see Fig. 2-left) were used to identify the oxidation state of surface copper species. The Cu 2p3/2 peak can typically be deconvoluted into components associated with Cu^0/Cu^+ (located at ~932–933 eV) and Cu^{2+} (expected at ~933.5–934.5 eV), the latter accompanied by characteristic shake-up satellites in the 941–945 eV range. The presence, absence, or relative intensity of these satellite features was used to discriminate between Cu(I)/Cu(0) and Cu (II). In our case, as can be seen clearly from Fig. 2 graphs, the absence of the Cu^{2+} satellite allows us to eliminate the Cu^{2+} component, leaving us with only metallic Cu or Cu1+ at 932.5 eV. To distinguish between these two options, we also acquired the Cu LMM Auger region (see Fig. 2-right), from which analysis, using the Modified Auger Parameter (MAP), the average oxidation state of the Cu present on the surface can be inferred. In our case, for the 2Cu–TiO_2 NM sample, we were able to fit the region (not shown) obtaining the value of the Cu LMM peak, equal to 569.9 eV, which gives, together with the Cu2p3/2 peak at 932.5 eV, a MAP value of 1849.2 eV. In literature [] this value is attributed to Cu(I) oxide. It was not possible to proceed with the same procedure on the 2Cu–TiO_2 SAS sample, due to the small amount of Cu found on the material surface, in line with the hypothesis that this time it involves doping rather than a 'decoration' with nanoclusters or nanoparticles. In fact, both in the Cu2p and in the Cu LMM regions, the characteristic Cu peaks can barely be distinguished from the background noise of the signal, so a signal peak fitting procedure could not be applied.

The Ti 2p spectra (not reported) exhibit the characteristic doublet of Ti^{4+} in TiO_2, with Ti 2p3/2 typically located at ~458.4–458.9 eV and the corresponding Ti 2p1/2 at ~464.1–464.8 eV [Applied Surface Science 257 (2010) 887–898]. The Ti2p peak has significantly separated spin-orbit components: the splitting value varies depending on the chemical state ((Δmetal = 6.1 eV, Δnitride = 6.0 eV and Δoxide = 5.7 eV). All the 4 samples have shown a separation equals to 5.7 eV, thus confirming the oxide form. Moreover, apart from sample 2Cu–TiO2 NM, the other three samples have shown a single oxidation state component, for the Ti4+, with peaks located at 458.6 eV and 464.3 eV, respectively for the 2p3/2 and ½ components. Sample 2Cu–TiO2 NM exhibits a double component for both the Ti 2p3/2 and ½ orbitals. Apart from the Ti^{4+} at 458.4 eV, a second component is located at 459.7 eV. Since Ti3+ and Ti2+ are usually located at lower binding energies values, this shift toward higher BE values may indicate the presence of interfacial effects arising from the interaction between TiO_2 and Cu species (e.g., electronic perturbations, surface plasmon losses, Ti–*O*-X (X = Cu, Ni, Au …), charge transfer, …) [52]. For example, Wei et al., [53], stated "A shift of the Ti 2p binding energy to higher values indicates electron depletion in TiO_2 caused by charge transfer at the interface.", which, in our case, can be due to Cu_2O/TiO_2 hetero-junction interface. The O 1s signal typically contains a lattice oxygen (Ti–O–Ti) contribution from TiO_2 at ~529.5–530.2 eV, oxygen vacancies and/or surface oxygens with incomplete coordination at 530.8 – 531.4 eV, together with higher-energy components (~531–532.5 eV) attributable to surface hydroxyls or adsorbed species and water or adsorbates at 532.5–534 eV. In samples containing Cu(I) species (Cu_2O), lattice oxygen bound to Cu^+ can appear around ~530.0–530.5 eV, together with C–O components,

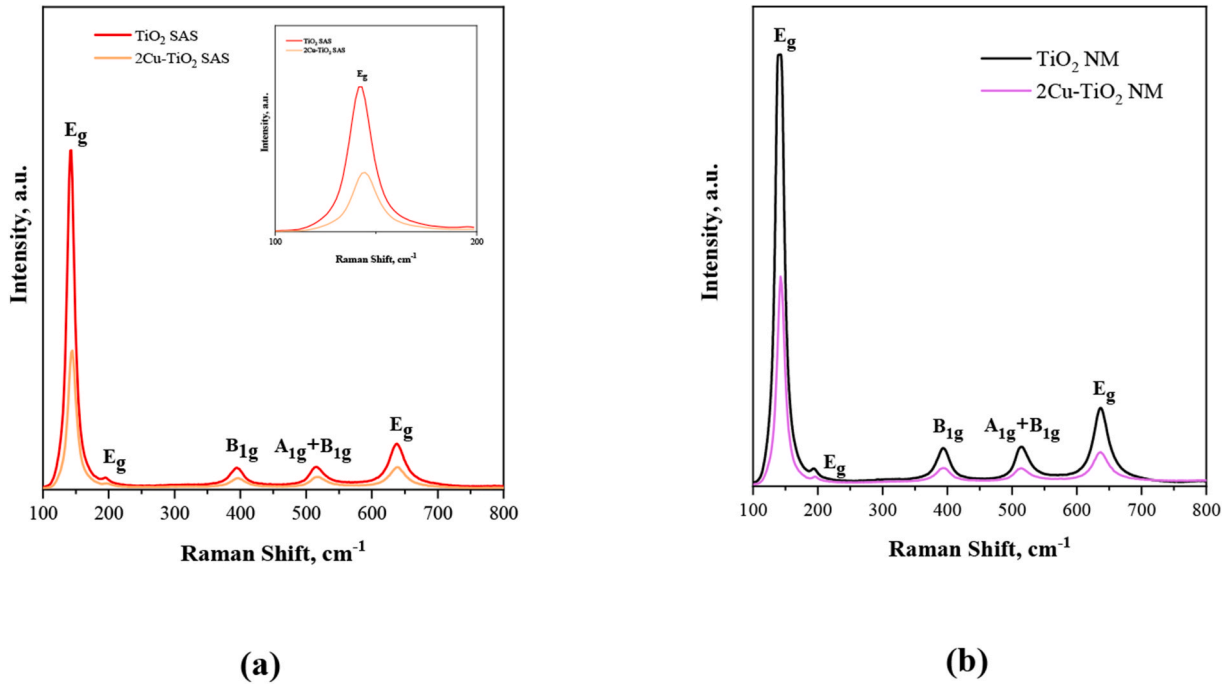

Fig. 5. (a) Raman spectra of TiO_2 SAS and 2Cu–TiO_2 SAS samples recorded in the 100–800 cm^{-1} (Inset: enlargement of the E_g mode at 144 cm^{-1}). (b) Raman spectra of TiO_2 NM and 2Cu–TiO_2 NM samples recorded in the 100–800 cm^{-1}.

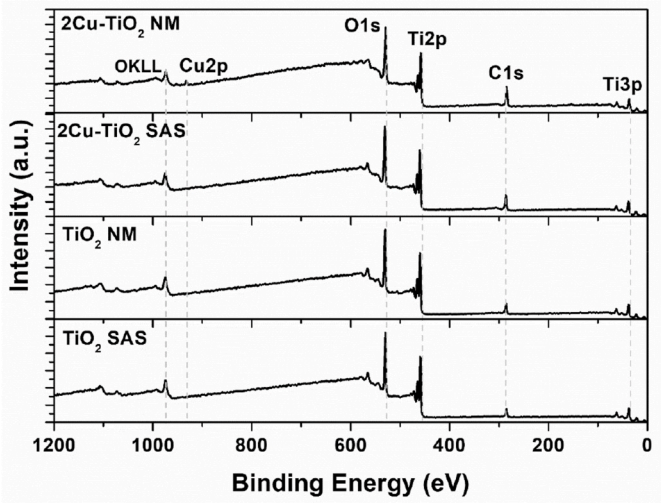

Fig. 6. XPS survey spectra for samples (from top to bottom): 2Cu–TiO_2 NM, 2Cu–TiO_2 SAS, TiO_2 NM, and TiO_2 SAS.

which belong to the same region. In Table 1 the results obtained from the fitting procedures applied to O 1s regions are reported (more parameters from these fitting procedures results are available in Table S1). Sample 2Cu–TiO_2 NM is the one which deviates the most from the average values reported for the other samples. This is since different components contribute to the O 1s signal, not only from TiO_2, but also from Cu_2O and the significant contamination from adventitious carbon, which also contains bonds with oxygen. For this reason, it is difficult to find a place for it within the value trend of the other three samples. In fact, for the remaining samples, it was possible to fit the O1s with only 3 components, excluding the adsorbate component, which is present only in the first sample. Among the other three samples, 2Cu–TiO_2 SAS is the one which exhibits the higher amount of defects and –OH components, which can promote lactic acid adsorption. The last region examined is the valence band one. The valence-band (VB) region provides insight into the electronic structure and the interaction between TiO_2 and surface species. The TiO_2 VB spectra are usually dominated by the O 2p and Ti 3d states, with a broad maximum between ~5 and 8 eV and a valence-band maximum (VBM) located around 2.8 eV (anatase) and 3.0-3.2 eV (rutile) below the Fermi level In our study, we can see from Fig. 3, that sample 2Cu–TiO2 NM has a different behaviour, since its VBM is located at 1.13 eV, while the other three samples show values in the range 2.68-2.78 eV, more in accordance with anatase-based

Table 2
XPS data related to the relative atomic concentration (at.%) of samples: 2Cu–TiO2 NM, 2Cu–TiO2 SAS, TiO2 NM and TiO2 SAS, together with O 1s regions peak fitting results and Modified Auger Parameters (MAP), calculated for each of the four samples.

Sample	Relative Atomic Concentration [at.%]				
	C1s	O1s		Ti2p	$Cu2p_{3/2}$
		Bonded with C	*Metal Oxide*		
2Cu–TiO_2 NM	36.5	16.1	29.1	17.6	0.7
2Cu–TiO_2 SAS	26.2	5.2	46.3	22.2	~0.1
TiO_2 NM	20.3	5.0	51.2	23.5	-
TiO_2 SAS	17.3	5.1	53.5	24.1	-

O 1s peak fitting data [%]				
	O from lattice (529.5-530.2 eV)	*O defects (530.8 – 531.4 eV)*	*-OH (531.5 – 532.0 eV)*	*Adsorbates (532.5 –534 eV)*
2Cu–TiO_2 NM	45.6	45.8	5.0	3.6
2Cu–TiO_2 SAS	79.5	11.9	8.6	-
TiO_2 NM	84.2	7.6	8.2	-
TiO_2 SAS	85.0	8.0	7.0	-

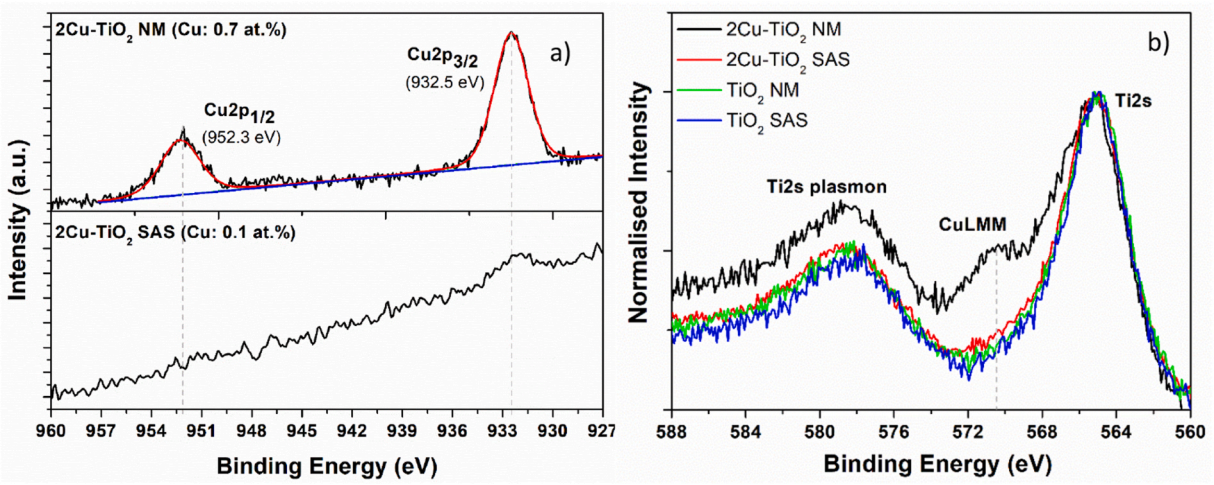

Fig. 7. (a) XPS (left) Cu2p HR spectra for 2Cu–TiO_2 NM (top) and 2Cu–TiO_2 SAS (bottom) samples; (b) Cu LMM-Ti2s region for 2Cu–TiO_2 NM, 2Cu–TiO_2 SAS, TiO_2 NM, and TiO_2 SAS.

compound. Huang et al. [54] have reported a shift towards the Fermi level for Cu_2O/TiO_2 heterojunctions interface, which reached values in the range 0.18-0.67 eV for Cu2O higher than 30 at.%, thanks to the Cu 3d filled states. In our samples, the relative amount of Cu is definitely lower, which implies a lower degree of variation of the VBM, due to Cu 3d electrons (See Fig. 8).

The UV–Vis diffuse reflectance spectra of all photocatalysts, expressed through the Kubelka–Munk function F(R), are shown in Fig. 9, and the corresponding band gap energies (E_{bg}) derived from Tauc plots (Fig. S3) are summarized in Table 3.

Both TiO_2 NM (3.30 eV) and TiO_2 SAS (3.25 eV) exhibit band-gap values fully consistent with those typically reported for anatase TiO_2 (≈3.2 ± 0.1 eV), confirming that the SAS process does not modify the intrinsic electronic structure of pure TiO_2 [55–57]. For both TiO_2 NM sample (Fig. 9a) and TiO_2 SAS (Fig. 9b), the absorption edge located at ~350 nm is characteristic of anatase and corresponds to the $O^{2-}(2p) \rightarrow Ti^{4+}(3d)$ charge-transfer transition [58].

A markedly different optical response is observed for the 2Cu–TiO_2 NM photocatalyst (Fig. 9a). This material displays broad absorption features extending well into the visible region (400–800 nm). The absorption shoulder between 450 and 515 nm is typically considered

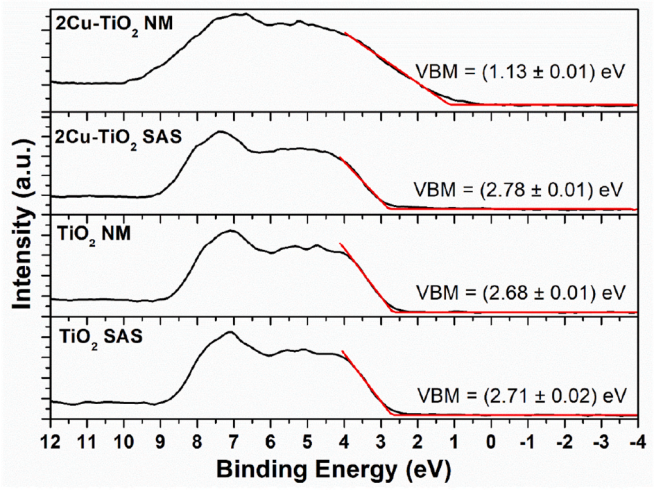

Fig. 8. XPS valence band regions for all the four samples. The VBM has been calculated by means of the "step-down" function, together with its uncertainties, thanks to Monte Carlo simulations. The final values are reported in each region.

evidence of Cu_2O–TiO_2 heterojunction formation [59]. Additionally, the broad absorption tail extending from 600 to 900 nm may be associated with electronic transitions in Cu_2O nanoclusters and plasmon-like absorption of metallic Cu nanoparticles supported on TiO_2, as reported for Cu^+/Cu^0–TiO_2 and Cu–TiO_2 systems displaying enhanced visible and near-infrared light harvesting [60,61]. This assignment is fully consistent with XPS results, which identify Cu exclusively as Cu^+/Cu^0 and exclude the presence of Cu^{2+}. Additionally, the broad absorption tail extending from 600 to 900 nm is characteristic of Cu_2O nanoclusters and metallic Cu plasmon-like absorption, frequently observed in Cu_2O/Cu composites supported on TiO_2 and generally attributed to intraband and defect-related transitions rather than to CuO-related d–d bands.

These visible-light absorption features appear only in the 2Cu–TiO_2 NM sample and are completely absent in SAS-derived catalyst, confirming that copper is not incorporated into the TiO_2 lattice in the sol–gel sample, but instead forms segregated Cu_2O/Cu surface domains.

As a consequence, the apparent band-gap value estimated for 2Cu–TiO_2 NM (1.55 eV) does not reflect a true narrowing of the TiO_2 band gap, but rather the convolution of the intrinsic optical transitions of Cu_2O (Eg ≈ 2.1 eV) and metallic Cu, which dominate the diffuse reflectance response and artificially shift the Tauc extrapolation toward lower energies [62].

Conversely, 2Cu–TiO2 SAS exhibits a moderate red shift of the absorption edge compared to TiO_2 SAS, 2.65 eV (Fig. 9b). This behavior is typically associated with lattice distortion and the formation of oxygen vacancies induced by Cu incorporation, which generate mid-gap states and slightly narrow the band gap [56]. The modest band-gap reduction observed for SAS-derived sample could be attributed to Cu-related defect states within the TiO_2 lattice, in line with Raman and lattice-parameter analyses.

The PL spectra of TiO_2 are typically characterized by emissions arising from shallow defect centres, whereas Cu-doped TiO_2 is dominated by deep-trap recombination processes. The incorporation of Cu^{2+} perturbs the local coordination environment of Ti^{4+} and promotes the formation of oxygen vacancies. These vacancies can trap photogenerated electrons and generate ionized oxygen-vacancy centres (F-type centres), which govern the main visible emission features. In particular, the 426 nm band originates from self-trapped excitons formed through interactions between Ti3d electrons and O2p holes [63]. The peak at 490 nm corresponds to F-centres with two trapped electrons, and the 536 nm emission is associated with deep-level recombination at F^+ centres [64,65]. Overall, the visible PL emission of Cu–TiO_2 can be ascribed to oxygen vacancies in different ionization states: F (two electrons), F^+ (one electron), and F^{2+} (no electrons) [66].

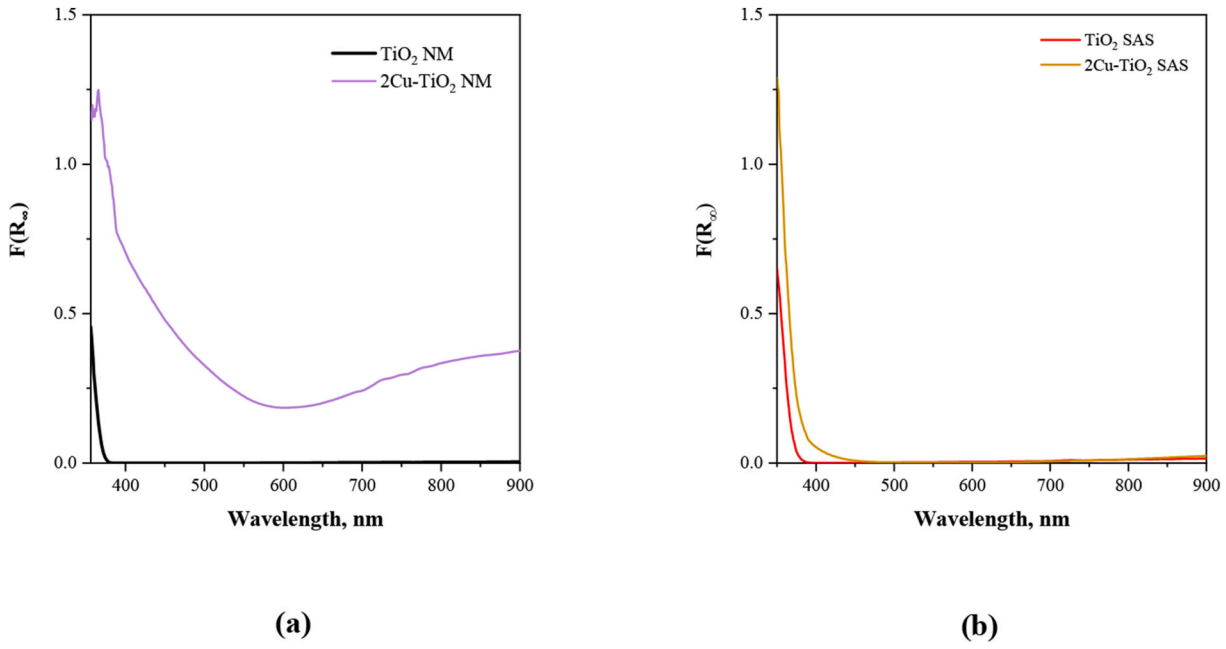

Fig. 9. UV–Vis diffuse reflectance spectra expressed as Kubelka–Munk function F(R) for: (a) TiO_2 NM and 2Cu–TiO_2 NM; (b) TiO_2 SAS and 2Cu–TiO_2 SAS.

Table 3
Band gap energies (E_{bg}) of TiO_2 NM, TiO_2 SAS, and Cu–TiO_2 photocatalysts calculated from Tauc plots using the Kubelka–Munk function.

Photocatalyst	E_{bg}, eV
TiO_2 NM	3.30
TiO_2 SAS	3.25
2Cu–TiO_2 NM	1.55
2Cu–TiO_2 SAS	2.65

The extent of electron trapping at these defect states significantly influences recombination processes and, consequently, photocatalytic performance. Both radiative and nonradiative pathways contribute to the observed PL efficiency. Oxygen vacancies located at grain boundaries typically are reported by Choudhury et al. to generate shallow trap levels below the conduction band and so acting as nonradiative recombination centres, reducing the PL contribution from shallow defects [64]. In contrast, Cu-related d-states and lattice oxygen vacancies deeper in the band gap favor radiative recombination and are responsible for the structured visible emission. Several effects may contribute to PL quenching, including the presence of high-density trap centres, grain-boundary defects, carrier mobility limitations, nonradiative Auger recombination, and concentration quenching.

Despite having an identical Cu loading, the two Cu–TiO_2 samples prepared through different routes exhibit markedly different PL responses (Fig. 10). The 2Cu–TiO_2 NM sample shows substantially lower PL intensity and less distinct emission peaks compared to 2Cu–TiO_2 SAS, with the spectral features appearing flattened over the emission band. This attenuation suggests a more prominent role of nonradiative recombination pathways, likely promoted by a higher concentration of structural defects or disordered regions. SEM, XPS and UV-Vis DRS analyses support this interpretation, revealing the presence of Cu-rich domains in the NM sample, which can act as efficient quenching centres and further suppress radiative transitions.

As summarized in Table S3, the 2Cu–TiO_2 SAS material exhibits a specific surface area (SSA) of 68.9 $m^2\ g^{-1}$ and a total pore volume of 0.702 $cm^3\ g^{-1}$. This relatively high surface area highlights the effectiveness of the supercritical antisolvent (SAS) process in producing finely dispersed nanostructured materials. In contrast, the sample

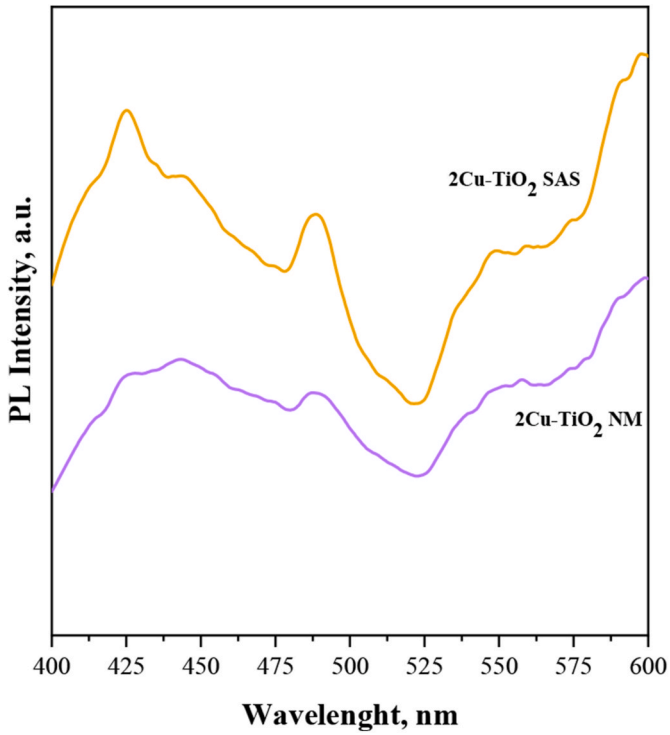

Fig. 10. Photoluminescence spectra of 2Cu–TiO_2 SAS and 2Cu–TiO_2 NM samples.

derived from the non-micronized precursor shows a significantly lower surface area, with values below 10 $m^2\ g^{-1}$, indicating a more compact structure likely resulting from particle aggregation and sintering during calcination. The 2Cu–TiO_2 SAS sample exhibits a Type II isotherm profile, typical of nonporous or macroporous materials (Fig. S4) [67]. The near-asymptotic increase in nitrogen uptake at high relative pressures (P/P°) suggests a pore structure predominantly composed of disordered mesopores to macropores formed between aggregated nanoparticles [68].

The combination of high surface area and interparticle porosity is expected to favor photocatalytic performance by enhancing the accessibility of active sites and improving mass transfer within the catalyst structure.

3.3. Photocatalytic hydrogen production

3.3.1. Influence of micronization and combination with Cu

The first set of photocatalytic experiments was carried out to evaluate the effect of micronization on the activity of TiO_2 under visible-light irradiation. Reactions were performed for 4 h using 1 g L^{-1} of catalyst and a 16 vol% lactic acid solution. A photolysis test (lactic acid only, no catalyst) was also performed under the same conditions for comparison. The results are reported in Fig. 11.

As expected, both undoped photocatalysts exhibited negligible activity under visible light. This behavior is consistent with their band gaps (3.30 eV for TiO_2 NM and 3.25 eV for TiO_2 SAS), which fall within the typical range of anatase TiO_2 and therefore require UV excitation [55,57]. For this reason, H_2 production obtained with TiO_2 NM (2859 μmol L^{-1}) and TiO_2 SAS (2886 μmol L^{-1}) was essentially comparable to photolysis (2738 μmol L^{-1}).

A remarkable improvement in hydrogen production was observed for both Cu-modified samples (Fig. 11). However, the magnitude and origin of this enhancement differ depending on the synthesis route. The 2Cu–TiO_2 NM photocatalyst displayed a substantial increase in H_2 evolution (3532 μmol L^{-1}). UV–Vis DRS (Fig. 9a) revealed absorption bands attributable to Cu_2O–TiO_2 charge-transfer transitions and d–d transitions of Cu^{2+}, respectively, features typical of segregated Cu_2O/CuO domains [58,69]. These secondary Cu-based oxides form efficient heterojunctions with TiO_2, favouring charge separation and boosting visible-light activity [70–72]. Indeed, the extremely low apparent band gap (1.55 eV, Table 3) is consistent with the optical response of CuO (1.4 eV) and Cu_2O (2.1 eV), rather than with true TiO_2 band-gap narrowing. In contrast, the 2Cu–TiO_2 SAS photocatalyst exhibited the highest performance (4040 μmol L^{-1}). In this material, copper is incorporated into the TiO_2 lattice, as confirmed by the XRD shift of the anatase (101) peak, the increase in lattice parameter *c*, and the Raman blue shift of the E_g Raman mode. The incorporation of Cu^{2+} and the associated formation of oxygen vacancies give rise to mid-gap defect states responsible for the observed band-gap narrowing (2.65 eV), enabling effective visible-light absorption [73]. Although XRD detected traces of Ti_2O_3, these reduced Ti species can facilitate charge transport and further enhance photocatalytic performance [74,75].

In addition, XPS and PL analyses consistently show that the SAS process produces a more active Cu-combined photocatalyst under visible light. In the SAS sample, Cu is incorporated into the TiO_2 lattice, creating beneficial oxygen vacancies and surface –OH groups that improve charge separation and substrate adsorption. The corresponding PL features associated with F, F^+, and F^{2+} centres indicate well-defined radiative defect states that help manage photogenerated carriers.

Overall, these results demonstrate that both Cu addition and micronization strongly influence photocatalytic behavior. The SAS-derived photocatalyst gains its superior performance from genuine band-gap engineering and oxygen-vacancy formation. This synergistic combination results in the highest H_2 production observed among all tested photocatalysts.

3.3.2. Influence of photocatalyst dosage

The photocatalyst dosage is a critical operational parameter that directly influences light–matter interaction, photon absorption, and overall reaction kinetics in heterogeneous photocatalysis. To identify the optimal catalyst loading, the most active material (2Cu–TiO_2 SAS) was tested at different dosages (0.5–2 g L^{-1}) under visible-light irradiation while keeping the lactic acid concentration fixed at 16 vol%. The results are reported in Fig. 12.

Hydrogen production increases from 2740 μmol L^{-1} at a dosage of 0.5 g L^{-1} to a maximum of 4040 μmol L^{-1} at 1 g L^{-1}, demonstrating that an increased number of active sites and enhanced photon absorption initially promote photocatalytic efficiency. However, when the catalyst dosage is further increased to 2 g L^{-1}, H_2 production decreases to 3820 μmol L^{-1}, indicating that excessive catalyst concentration becomes detrimental to the process.

This behaviour is fully consistent with previous findings reported in

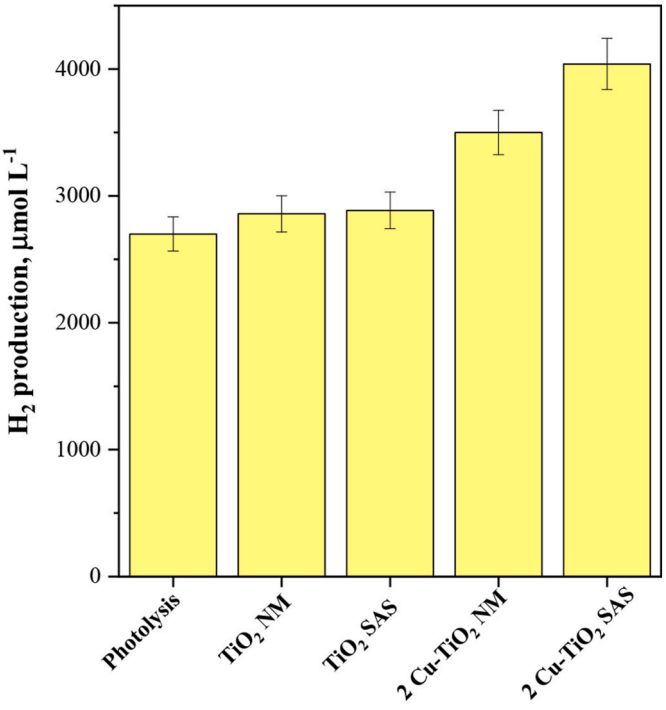

Fig. 11. H_2 production after 4 h of visible-light irradiation using 16 vol% lactic acid and a catalyst dosage of 1 g L^{-1}. Comparison between photolysis, non-micronized TiO_2 (TiO_2 NM), SAS-micronized TiO_2 (TiO_2 SAS), non-micronized Cu-doped TiO_2 (2Cu–TiO_2 NM), and SAS-derived Cu-doped TiO_2 (2Cu–TiO_2 SAS).

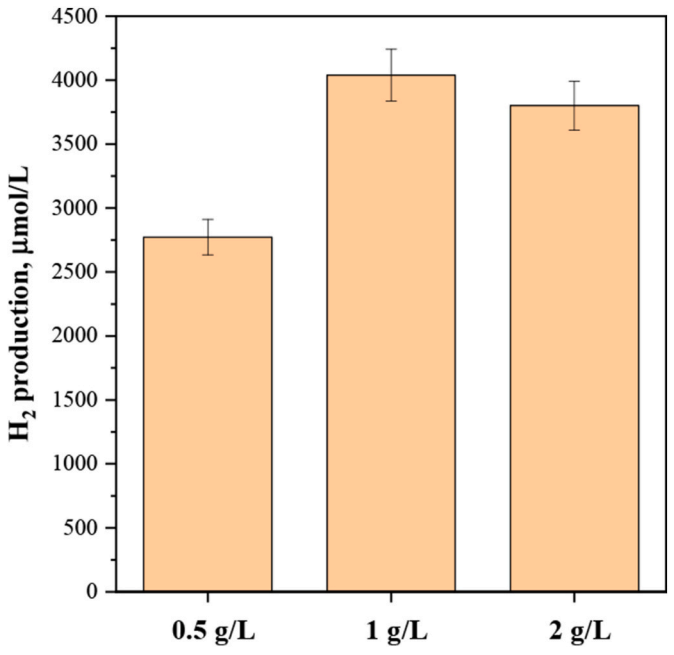

Fig. 12. H_2 production after 4 h of visible irradiation using 2Cu–TiO_2 SAS at different photocatalyst dosages.

the literature. Higher photocatalyst dosages increase the turbidity and opacification of the suspension, thereby limiting light penetration through the aqueous phase and reducing the effective photon flux reaching the active surface [76,77]. Moreover, elevated solid concentrations favor particle agglomeration, which reduces the accessible surface area and diminishes the active interfacial sites participating in the photocatalytic reaction [78].

Overall, these results indicate that 1 g L^{-1} represents the optimal trade-off between maximizing photon absorption and minimizing light scattering and aggregation phenomena.

3.3.3. Influence of lactic acid concentration and kinetic considerations

Additional photocatalytic experiments were carried out to investigate the influence of lactic acid concentration on hydrogen evolution. Lactic acid acts as an effective electron donor, rapidly scavenging photogenerated holes and thereby suppressing electron–hole recombination on the semiconductor surface. The most active photocatalyst, 2Cu–TiO_2 SAS at the optimal dosage of 1 g L^{-1}, was selected for this study. A control experiment performed in the absence of lactic acid confirmed that hydrogen was still produced (1750 μmol L^{-1}), attributable to photocatalytic water splitting.

Lactic acid concentrations of 4, 8, 16, and 40 vol% were tested, and the results (Fig. 14) show that H_2 evolution increases progressively with lactic acid concentration up to 16 vol%, at which the maximum hydrogen production (4040 μmol L^{-1}) is achieved. Further increasing the sacrificial agent concentration to 40 vol% leads to a noticeable decrease in H_2 production (3214 μmol L^{-1}),. This reduction in photocatalytic hydrogen production at concentrations above 16 vol% cannot be attributed to an increased aggregation of catalyst particles in suspension. Fig. S5 shows a progressive decrease in the average aggregate size with increasing lactic acid concentration, form 2672 nm at 4 vol% to 636 nm at 40 vol%. This behaviour is consistent with the increase in the absolute value of the Z-potential observed at higher lactic acid concentration. Since the Z-potential is strongly pH dependent, the progressive acidification of the solution shifts the system away from the point of zero charge density and enhanced electrostatic repulsion between particles. Consequently, electrostatic stability is improved and particle aggregation is reduced. Therefore, the observed reduction in H_2 production at higher lactic acid concentrations is more likely related to surface-related phenomena, such as competitive adsorption of lactic acid and/or reaction intermediates on the photocatalyst surface, leading to a partial blockage of active sites and a consequent limitation of charge transfer and proton reduction kinetics.

The dependence of hydrogen production on the initial lactic acid concentration was described using a substrate inhibition kinetic model of the Andrews–Haldane type, which is suitable for systems exhibiting an increase in reaction rate up to an optimum substrate concentration followed by a decline at higher concentrations [79,80]. The adopted kinetic expression is:

$$r = r_0 + \frac{r_{max}\cdot[C]}{K_s + [C] + \frac{[C]^2}{K_I}} \qquad \text{Eq.(3)}$$

Where r_0 represents the background rate, i.e. the contribution arising from pathways that do not depend on substrate adsorption (such as direct water splitting) [81]; r_{max} is the maximum theoretical hydrogen production rate, K_S is the semi-saturation constant, K_I is the substrate inhibition constant, and [C] is the initial lactic acid concentration. In this model, the quadratic inhibitory term $\frac{[C]^2}{K_I}$ accounts for substrate-induced suppression effects that become significant at high lactic acid concentrations. At low substrate concentrations, the hydrogen production rate increases nearly linearly with [C], mainly due to the enhanced scavenging of photogenerated holes by lactic acid, which reduces charge carrier recombination. As the concentration increases further, the reaction rate approaches a maximum value corresponding to an optimal balance between substrate availability and surface reactivity. At very high lactic acid concentrations, inhibitory effects become dominant, resulting in a decrease in hydrogen production. From a photocatalytic perspective, this inhibition behavior may be associated with several concurrent phenomena, including saturation or blocking of catalyst active sites, competitive adsorption between lactic acid, water, and reaction intermediates, local pH modifications at the catalyst surface, light screening effects, and quenching of reactive photogenerated species. The Andrews–Haldane formulation therefore successfully describes the characteristic non-monotonic trend experimentally observed in Fig. 13, consisting of an initial increase in hydrogen production, followed by a maximum and a subsequent decrease at higher substrate concentrations. The kinetic parameters r_{max}, K_S, and K_I were determined by nonlinear least-squares regression of the experimental hydrogen production rates as a function of lactic acid concentration. The resulting values are reported in Table 4.

The model reproduces the experimental trend satisfactorily (Fig. 13), yielding a coefficient of determination $R^2 = 0.9359$. RMSE was calculated based on the deviation between experimental and model-predicted hydrogen production values.

To further assess the predictive capability of the proposed preliminary kinetic model, additional photocatalytic tests were carried out at intermediate lactic acid concentrations of 6 vol% and 32 vol%. These concentrations were not included in the parameter-fitting dataset and therefore served as external validation points. The corresponding experimental H_2 production values were compared with the model predictions obtained using the kinetic parameters previously estimated (Fig. 14). The comparison demonstrates that the model retains a high predictive accuracy, with an excellent correlation between experimental and calculated values.

3.3.4. Role of water in the reaction mechanism and possible reaction mechanism for the photocatalytic hydrogen production with 2Cu–TiO_2 SAS

To elucidate the contribution of water to the overall reaction mechanism, a photocatalytic test was performed by replacing distilled water with deuterated water (D_2O) while keeping constant the catalyst (2Cu–TiO_2 SAS), dosage (1 g L^{-1}), and lactic acid concentration (16 vol %). As shown in Fig. 15, the use of D_2O led to a decrease in both hydrogen and carbon dioxide production. Hydrogen formation decreased moderately from 4040 μmol L^{-1} (H_2O) to 3200 μmol L^{-1}

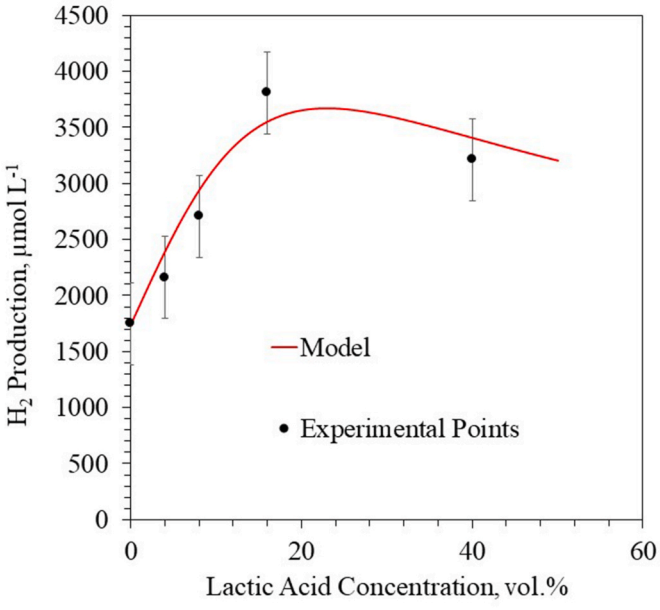

Fig. 13. Experimental hydrogen production after 4 h of visible-light irradiation using 2Cu–TiO_2 SAS at different lactic acid concentrations (4–40 vol%).

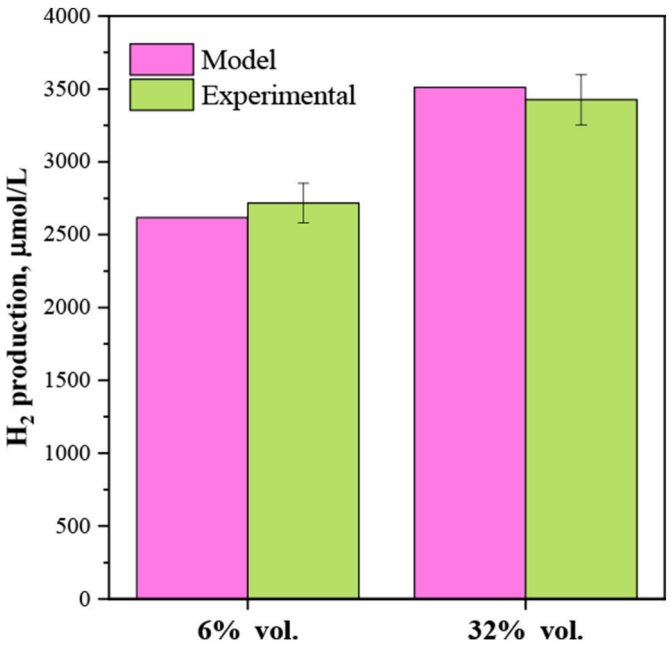

Fig. 14. Comparison between the H_2 production predicted by the modified Langmuir–Hinshelwood model and the corresponding experimental values at lactic acid concentrations of 6 vol% and 32 vol%.

Table 4
Kinetic parameters obtained from fitting the experimental hydrogen production rates using the modified Langmuir–Hinshelwood model. In the table, "LA" refers to lactic acid.

r_0, $\mu mol_{H2}/(h*g_{cat})$	r_{max}, $\mu mol_{H2}/(h*g_{cat})$	K_S, mol/L_{LA}	K_I, mol/L_{LA}
1750	$3.62*10^6$	$2.6*10^3$	$3.02*10^{-3}$

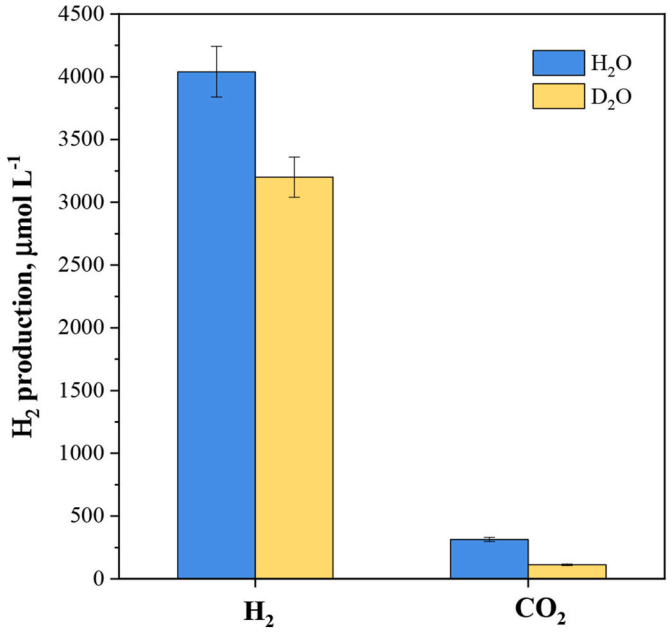

Fig. 15. Comparison of H_2 and CO_2 production after 4 h of visible-light irradiation using the 2Cu–TiO_2 SAS photocatalyst in the presence of either H_2O or D_2O as solvent.

(D_2O), whereas CO_2 production exhibited a much more significant drop.

These observations clearly confirm that lactic acid serves as the primary hydrogen source, acting as an efficient electron donor under visible-light irradiation [82]. The reduced but still appreciable H_2 production in D_2O indicates that water also may participate in the proton-supply step for molecular hydrogen formation. The decrease in CO_2 formation further suggests that the oxidative degradation of lactic acid strongly depends on reactive oxygen species generated from water oxidation. Lactic acid is likely first converted into intermediate species, such as pyruvic acid, before undergoing deeper oxidation into CO_2. The suppressed formation of reactive oxygen species in D_2O slows down these oxidation steps, resulting in lower CO_2 yields [83].

The electronic structure of the 2Cu–TiO_2 SAS photocatalyst was evaluated to support the proposed reaction mechanism. Specifically, the valence band edge (E_{VB}) and conduction band edge (E_{CB}) positions at pH = 2.1 (the spontaneous pH of the lactic acid solution) were estimated using the Mulliken electronegativity approach combined with the Nernst equation (Eq. (4) and Eq. (5)):

$$E_{VB} = \chi - 4.5 + 0.5*E_{bg} - 0.059*pH \quad \text{Eq.(4)}$$

$$E_{CB} = E_{VB} - E_g \quad \text{Eq.(5)}$$

The proposed sequence of reactions is reported below and schematically illustrated in Fig. 16.

$$Cu - TiO_2 + h\nu \rightarrow Cu - TiO_2\ (e^- + h^+) \quad \text{Eq.(6)}$$

$$C_3H_6O_3 + 2h^+ \rightarrow \text{Intermediates} + 2H^+ \quad \text{Eq.(7)}$$

$$2H_2O + 4h^+ \rightarrow O_2 + 4H^+ \quad \text{Eq.(8)}$$

$$2H^+ + 2e^- \rightarrow 2H^{\cdot} \quad \text{Eq.(9)}$$

$$H^{\cdot} + H^{\cdot} \rightarrow H_2 \quad \text{Eq.(10)}$$

$$\text{Intermediates} \rightarrow CO_2 \quad \text{Eq.(11)}$$

Using the experimentally determined band-gap value, the calculated potentials for 2Cu–TiO_2 SAS at pH = 2.1 are +2.36 V for E_{VB} and −0.335 V for E_{CB}. Under visible-light irradiation, photoexcitation promotes electrons from the VB to the CB, generating electron–hole pairs that drive reductive and oxidative half-reactions (Eq. (6)). The valence band edge of 2Cu–TiO_2 SAS estimated from XPS (≈+2.5 V vs NHE at pH 2.1) is in good agreement with the value calculated using the Mulliken electronegativity approach, confirming the reliability of the proposed band alignment.

On the photocatalyst surface, both lactic acid and water compete for adsorption. The TiO_2 surface is inherently hydrophilic and readily forms hydrogen bonds with surface hydroxyl groups. At pH = 2.1, lactic acid (pKa = 3.86) is predominantly present in its protonated –COOH form, which can interact with TiO_2 via hydrogen bonding, though weaker than

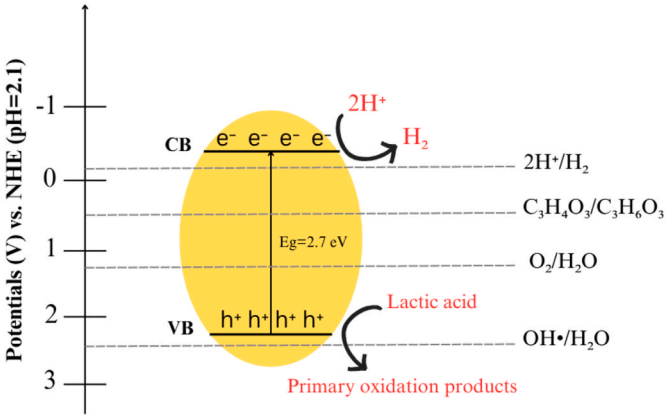

Fig. 16. Proposed photocatalytic mechanism in the presence of 2Cu–TiO_2 SAS.

water [84]. This selective adsorption affects the local concentration of reactants involved in oxidation.

The oxidation potential required for •OH radical formation is approximately +2.38 V vs NHE at pH = 2.1, while the potential for the oxygen evolution reaction (OER) is +1.105 V vs NHE under the same conditions [85]. Therefore, photogenerated holes in 2Cu–TiO_2 SAS (+2.36 V) are thermodynamically capable of oxidizing water via OER (Eq. (8)) but they are not able to generate •OH from water.

Moreover, the standard redox potential for the lactic acid/pyruvic acid couple is not directly tabulated, but the pyruvate/lactate couple ($E^\circ \approx -0.19$ V vs NHE at pH 7) is well-established [86]. Applying the Alberty pH-dependent thermodynamic transformation to adjust this potential to pH = 2.1 yields an apparent oxidation potential of approximately +0.48 V vs NHE [87]. Because this value is significantly lower than the VB potential of 2Cu–TiO_2 SAS, oxidation of lactic acid by photogenerated holes (Eq. (10)) is strongly favored over water oxidation. The oxidation of lactic acid by photogenerated holes led to the formation of partially oxidized organic intermediates and the release of protons (Eq. (7)). In parallel, water molecules also undergo oxidative activation by holes, generating oxygen and additional protons (despite in al lower extent), as shown in Eq. (8). The photogenerated electrons accumulated in the conduction band participate in the proton reduction reaction, producing surface-bound hydrogen radicals (H•) according to Eq. (11). Finally, H• recombine to form molecular hydrogen, as described in Eq. (10).

Based on these considerations, photogenerated holes preferentially oxidize lactic acid, generating partially oxidized intermediates. Moreover, surface-bound oxidizing species (likely originating from water oxidation rather than free ·OH radicals) assist in the deeper oxidation and decarboxylation of lactic-acid intermediates, ultimately leading to CO_2 formation (Eq. (11)). The strong suppression of CO_2 formation observed in D_2O experiments confirms that water-derived oxidative steps. However, the contribution of water to the overall oxidative pathway is minor compared to that of lactic acid, as evidenced by the limited decrease in H_2 production observed when H_2O is replaced with D_2O. This indicates that lactic acid is the primary electron donor and the dominant source of protons, whereas water mainly provides a secondary proton reservoir.

3.3.5. *Comparison with the existing literature*

A comparative analysis was carried out using available literature studies on photocatalytic hydrogen production from lactic acid. To improve consistency among different experimental conditions, the H_2 yields reported in the literature were normalized with respect to incident light power, catalyst mass, and the moles of lactic acid. These parameters were selected because they strongly influence photocatalytic activity, affecting photon availability, the number of active sites, and the overall process efficiency. The values extracted from the literature are summarized in Table 5, while the normalized hydrogen production rates are reported in Fig. 17.

As shown in Fig. 17, the photocatalyst developed in this study exhibits among the highest normalized hydrogen production values compared to the selected literature reports. In particular, a hydrogen production of 941 μmol H_2 $g(cat)^{-1}$ W^{-1} $mol(LA)^{-1}$ was obtained under visible-light irradiation. This value is higher than those reported for several CdS-based photocatalysts and C/TiO_2 systems considered in this comparison. However, it should be emphasized that such comparisons are intended as a normalized benchmark rather than a direct performance ranking, due to unavoidable differences in experimental setups.

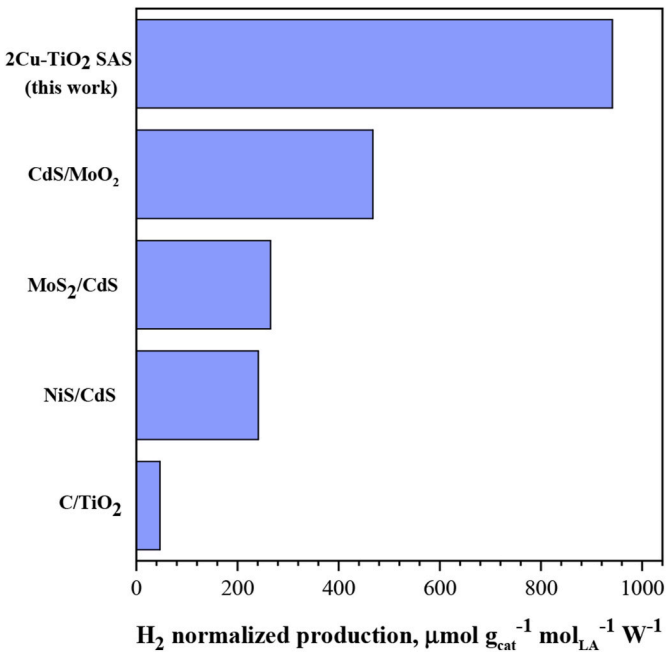

Fig. 17. Comparison of normalized H_2 production rates for the 2Cu–TiO_2 SAS photocatalyst developed in this work and selected photocatalysts reported in the literature.

Literature studies on Cu-based TiO_2 systems indicate that alcohols such as methanol and glycerol generally lead to higher hydrogen evolution efficiencies, whereas carboxylic acids (e.g., formic and lactic acid) typically result in lower performances [82,92,93]. Nevertheless, when compared with commonly used sacrificial agents (methanol, triethanolamine, glycerol, and isopropanol), the photocatalyst developed in this work falls within the upper range of reported normalized productivities (Table 6).A higher normalized hydrogen production rate has been reported in the presence of isopropanol [98]. however, it should be noted that those experiments were conducted under UV irradiation, which significantly affects photocatalytic activity. Overall, these results highlight the good photocatalytic performance of the SAS-derived Cu–TiO_2 material under visible-light conditions and its potential for hydrogen production from biomass-derived organic substrates.

4. Conclusions

In this work, Cu-doped TiO_2 photocatalysts were successfully synthesized using the Supercritical Antisolvent (SAS) technique, demonstrating that micronization under supercritical CO_2 is an effective strategy to tune the structural and electronic properties of TiO_2 for visible-light photocatalysis. Compared to conventional sol–sol-gel-derived materials, SAS-micronized photocatalysts exhibited nanometric morphology, improved dopant dispersion, and clear evidence of lattice distortion along the c-axis, confirming the effective incorporation

Table 5
Literature papers on the photocatalytic production of H_2 from lactic acid, considering 4 h of irradiation.

Photocatalyst	Light Source	Lactic Acid Concentration, % vol.	Photocatalyst Concentration, g L^{-1}	Reference
MoS_2/CdS	300 W Xenon Lamp with a cut-off filter (λ > 420 nm)	10	0.5	[88]
NiS/CdS	300 W Xenon Lamp with a cut-off filter (λ > 420 nm)	30	3	[89]
C/TiO_2	300 W Xenon Lamp with a cut-off filter (λ > 420 nm)	4	0.3	[90]
CdS/MoO_2	300 W Xenon Lamp	10	0.5	[91]
2Cu–TiO_2 SAS	Philips, 32 W, 400 nm < λ < 600 nm	16.7	1	This work

Table 6
Literature papers on the photocatalytic production of H_2 using Cu-based TiO_2 photocatalysts in the presence of different sacrificial agents (SA), considering 4 h of irradiation.

Sacrificial Agent (SA)	Light Source	SA Concentration, vol. %	Photocatalyst Concentration, g L^{-1}	H_2 normalized production, μmol g_{cat}^{-1} W^{-1}	Reference
Methanol	300 W Xe lamp (Simulated solar light)	25	0.125	83.8	[94]
Triethanolamine	300 W Xe lamp (Simulated solar light)	10	0.0714	44.6	[95]
Methanol	1000 W Xe lamp (Simulated solar light)	10	1.25	7.31	[96]
Glycerol	300 W Xe lamp (Simulated solar light)	5.4	8	8.64	[97]
Isopropyl alcohol	100 W Hg lamp (UV light)	10	1	135	[98]
Lactic acid	32 W (Visible light)	16	1	126	This Work

of Cu into the anatase framework. Among the prepared materials, 2Cu–TiO_2 SAS showed the highest performance, achieving 4040 μmol L^{-1} of H_2 after 4 h of visible irradiation. Raman spectroscopy, XRD analysis, UV–vis diffuse reflectance, and XPS analysis consistently indicated that the 2Cu–TiO_2 SAS photocatalyst achieves the most effective incorporation of Cu into the TiO_2 lattice. The homogeneous introduction of Cu into TiO_2 obtained through SAS leads to controlled band gap narrowing, enhanced visible light absorption, and the formation of beneficial defect states, such as oxygen vacancies and surface –OH groups, that promote substrate absorption and create electronically favourable trap levels for charge separation. PL analysis further supports this interpretation since it shows structured missions associated with defects and oxygen-vacancy centres, indicative of radiative defect states that assist charge management. In contrast, the non-micronized counterpart displays strong PL quenching due to Cu-rich surface aggregates acting as deep non-radiative recombination centres, consistent with XPS and UV-Vis diffuse reflectance observations. Photocatalytic experiments performed in D_2O demonstrated that lactic acid is the primary electron donor, while water plays a minor yet essential role as a secondary proton reservoir. The kinetic behavior of the system was described through a modified Langmuir–Hinshelwood model incorporating an inhibition term at high lactic acid concentrations. The model reproduced experimental trends with excellent agreement ($R^2 = 0.936$) and reliably predicted hydrogen evolution under intermediate lactic acid concentrations. Finally, when normalized to catalyst mass, incident-light power, and lactic-acid moles, the 2Cu–TiO_2 SAS photocatalyst achieved a hydrogen production rate of 941 $\mu mol_{H2}\, g_{catalyst}^{-1}\, W^{-1}\, mol_{LA}^{-1}$ a value significantly higher than state-of-the-art TiO_2- or CdS-based materials reported in the literature. Overall, this study demonstrates that SAS micronization combined with controlled Cu doping offers a powerful route to engineer TiO_2 photocatalysts with superior visible-light activity. The insights gained into dopant incorporation, defect formation and reaction kinetics provide a comprehensive foundation for the rational design of next-generation photocatalysts for solar-driven hydrogen production from renewable organics.

CRediT authorship contribution statement

Maria Chiara Iannaco: Formal analysis, Investigation, Writing – original draft. **Giuseppina Iervolino:** Data curation, Methodology, Supervision, Writing – review & editing. **Serena Esposito:** Conceptualization, Data curation, Visualization, Writing – review & editing. **Andrea Muscatello:** Formal analysis, Visualization. **Micaela Castellino:** Data curation, Formal analysis, Writing – review & editing. **Iolanda De Marco:** Conceptualization, Writing – review & editing. **Vincenzo Vaiano:** Conceptualization, Data curation, Methodology, Visualization, Writing – review & editing.

Declaration of competing interest

The authors declare that they have no known competing financial interests or personal relationships that could have appeared to influence the work reported in this paper.

Appendix A. Supplementary data

Supplementary data to this article can be found online at https://doi.org/10.1016/j.ijhydene.2026.155955.

References

[1] Council TPP. Frequently asked questions (FAQ). 2016.
[2] Khatib H. IEA World Energy Outlook 2011—A comment. Energy Policy 2012;48:737–43.
[3] Corredor J, Rivero MJ, Rangel CM, Gloaguen F, Ortiz I. Comprehensive review and future perspectives on the photocatalytic hydrogen production. J.J.o.C.T. Biotechnology 2019;94:3049–63.
[4] Puga AV. Photocatalytic production of hydrogen from biomass-derived feedstocks. Coord Chem Rev 2016;315:1–66.
[5] Lettieri S, Pavone M, Fioravanti A, Santamaria Amato L, Maddalena P. Charge carrier processes and optical properties in TiO2 and TiO2-Based heterojunction photocatalysts. A Review, Materials 2021;14:1645.
[6] Lin JC-T, Sopajaree K, Jitjanesuwan T, Lu M-C. Application of visible light on copper-doped titanium dioxide catalyzing degradation of chlorophenols. Sep Purif Technol 2018;191:233–43.
[7] Umebayashi T, Yamaki T, Itoh H, Asai K. Band gap narrowing of titanium dioxide by sulfur doping. Appl Phys Lett 2002;81:454.
[8] Christoforidis KC, Fernández-García MJCS. Photoactivity and charge trapping sites in copper and vanadium doped anatase TiO 2 nano-materials. Technology 2016;6:1094–105.
[9] Mathew S, Ganguly P, Rhatigan S, Kumaravel V, Byrne C, Hinder SJ, Bartlett J, Nolan M, Pillai SC. Cu-doped TiO2: visible light assisted photocatalytic antimicrobial activity. Appl Sci 2018;8:2067.
[10] Guo M, Du J. First-principles study of electronic structures and optical properties of Cu, Ag, and Au-doped anatase TiO2. Phys B Condens Matter 2012;407:1003–7.
[11] Liu C, Liu Z, Zhu Y. Comparison of the photocatalytic efficience for Cu and N Co-Doped TiO2 by Sol-Gel and xerogel-hydrothermal methods. Mater Trans 2018;59:811–5.
[12] Preda S, Pandele-Cuşu J, Petrescu SV, Ciobanu EM, Petcu G, Culiță DC, Apostol NG, Costescu RM, Raut I, Constantin M. Photocatalytic and antibacterial properties of doped TiO2 nanopowders synthesized by sol– gel method. Gels 2022;8:673.
[13] Tryba B, Orlikowski J, Wróbel R, Przepiórski J, Morawski AW. Performance, preparation and characterization of rutile-type TiO2 doped with Cu. J Mater Eng Perform 2015;24:1243–52.
[14] Jiang D, Otitoju TA, Ouyang Y, Shoparwe NF, Wang S, Zhang A, Li S. A review on metal ions modified TiO2 for photocatalytic degradation of organic pollutants. Catalysts 2021;11:1039.
[15] Franco P, Sacco O, De Marco I, Vaiano V. Zinc oxide nanoparticles obtained by supercritical antisolvent precipitation for the photocatalytic degradation of Crystal Violet dye. Catalysts 2019;9:346.
[16] Mottola S, Mancuso A, Sacco O, Vaiano V, De Marco I. Photocatalytic systems based on ZnO produced by supercritical antisolvent for ceftriaxone degradation. Catalysts 2023;13:1173.
[17] Franco P, Navarra W, Sacco O, De Marco I, Mancuso A, Vaiano V, Venditto V. Photocatalytic degradation of atrazine under visible light using Gd-doped ZnO prepared by supercritical antisolvent precipitation route. Catal Today 2022;397–399:240–8.
[18] Mancuso A, Sacco O, Mottola S, Pragliola S, Moretta A, Vaiano V, De Marco I. Synthesis of Fe-doped ZnO by supercritical antisolvent precipitation for the degradation of azo dyes under visible light. Inorg Chim Acta 2023;549:121407.
[19] Lima JPP, Aguiar A. Evaluating the performance of a wastewater treatment plant of a dairy facility in Southern Minas Gerais, Brazil. Sustainability 2025;17:7597.
[20] Castillo Martinez FA, Balciunas EM, Salgado JM, Domínguez González JM, Converti A, Oliveira RPdS. Lactic acid properties, applications and production: a review. Trends Food Sci Technol 2013;30:70–83.
[21] Reverchon E, De Marco I. Mechanisms controlling supercritical antisolvent precipitate morphology. Chem Eng J 2011;169:358–70.
[22] Mancuso A, Sacco O, Sannino D, Pragliola S, Vaiano V. Enhanced visible-light-driven photodegradation of Acid Orange 7 azo dye in aqueous solution using Fe-N co-doped TiO2. Arab J Chem 2020;13:8347–60.
[23] Vinila VS, Isac J. Chapter 14 - synthesis and structural studies of superconducting perovskite GdBa2Ca3Cu4O10.5+δ nanosystems. In: Thomas S, Kalarikkal N,

Abraham AR, editors. Design, fabrication, and characterization of multifunctional nanomaterials. Elsevier; 2022. p. 319–41.
[24] Iannaco MC, Mottola S, Vaiano V, Iervolino G, De Marco I. CeO2-CuO composites prepared via supercritical antisolvent precipitation for photocatalytic hydrogen production from lactic acid aqueous solution. J CO2 Util 2024;85:102878.
[25] Lu T, Blackburn S, Dickinson C, Rosseinsky MJ, Hutchings G, Axon S, Leeke GA. Production of titania nanoparticles by a green process route. Powder Technol 2009; 188:264–71.
[26] Marin RP, Ishikawa S, Bahruji H, Shaw G, Kondrat SA, Miedziak PJ, Morgan DJ, Taylor SH, Bartley JK, Edwards JK, Bowker M, Ueda W, Hutchings GJ. Supercritical antisolvent precipitation of TiO2 with tailored anatase/rutile composition for applications in redox catalysis and photocatalysis. Appl Catal Gen 2015;504:62–73.
[27] Reverchon E, De Marco I. Supercritical antisolvent micronization of Cefonicid: thermodynamic interpretation of results. J Supercrit Fluids 2004;31:207–15.
[28] Lengsfeld CS, Delplanque JP, Barocas VH, Randolph TW. Mechanism governing microparticle morphology during precipitation by a compressed antisolvent: atomization vs nucleation and growth. J Phys Chem B 2000;104:2725–35.
[29] Martín A, Cocero MJ. Numerical modeling of jet hydrodynamics, mass transfer, and crystallization kinetics in the supercritical antisolvent (SAS) process. J Supercrit Fluids 2004;32:203–19.
[30] Reverchon E, De Marco I, Torino E. Nanoparticles production by supercritical antisolvent precipitation: a general interpretation. J Supercrit Fluids 2007;43: 126–38.
[31] Akhtar T, Nasir H, Sitara E, Bukhari SAB, Ullah S, Iqbal RMA, Research P. Efficient photocatalytic degradation of nitrobenzene by copper-doped TiO2: kinetic study, degradation pathway, and mechanism. Environ Sci Pollut Control Ser 2022;29: 49925–36.
[32] Hu T, Feng P, Guo L, Chu H, Liu F. Construction of Built-In electric field in TiO2@ Ti2O3 core-shell heterojunctions toward optimized photocatalytic performance. Nanomaterials 2023;13:2125.
[33] Khan SR, Kanwal S, Hashaam M, Jamil S, Ullah B, Janjua MRSA. Investigation of catalytic and fuel additive applications of copper/copper (I) oxide/copper (II) oxide (Cu/CuO/Cu2O) microspheres synthesized by hydrothermal method using sucrose as template. Mater Res Express 2020;7:025036.
[34] Anitha B, Khadar MA. Dopant concentration dependent magnetism of Cu-doped TiO2 nanocrystals. J.J.o.N.R J Nanoparticle Res 2016;18:149.
[35] Praveen P, Viruthagiri G, Mugundan S, Shanmugam N. Structural, optical and morphological analyses of pristine titanium di-oxide nanoparticles – synthesized via sol–gel route. Spectrochim Acta Mol Biomol Spectrosc 2014;117:622–9.
[36] Chougala L, Yatnatti M, Linganagoudar R, Kamble R, Kadadevarmath J. A simple approach on synthesis of TiO2 nanoparticles and its application in dye sensitized solar cells. J Nano Electron Phys 2017;9(4). 04005-1-04005-6.
[37] Yamakawa K, Sato Y, Fukutani K. Asymmetric and symmetric absorption peaks observed in infrared spectra of CO2 adsorbed on TiO2 nanotubes. J.T.J.o.C.P. J Chem Phys 2016;144.
[38] Olurode K, Neelgund GM, Oki A, Luo Z. A facile hydrothermal approach for construction of carbon coating on TiO2 nanoparticles. Spectrochim Acta Mol Biomol Spectrosc 2012;89:333–6.
[39] Wang S, Meng KK, Zhao L, Jiang Q, Lian JS. Superhydrophilic Cu-doped TiO2 thin film for solar-driven photocatalysis. Ceram Int 2014;40:5107–10.
[40] Chen Y-K, Lin Y-F, Peng Z-W, Lin JL. Transmission FT-IR study on the adsorption and reactions of lactic acid and poly (lactic acid) on TiO2. J Phys Chem 2010;C114: 17720–7.
[41] Chen Y, Dong Q, Wang L, Guo X, Ai S, Ding H. Graphitic-C3N4 quantum dots decorated {001}-faceted TiO2 nanosheets as a 0D/2D composite with enhanced solar photocatalytic activity. Res Chem Intermed 2018;44:7369–89.
[42] Dhanalakshmi J, Iyyapushpam S, Nishanthi S, Malligavathy M, Padiyan DP. Investigation of oxygen vacancies in Ce coupled TiO2 nanocomposites by Raman and PL spectra. Adv Nat Sci Nanosci Nanotechnol 2017;8:015015.
[43] Mazzolini P, Russo V, Casari CS, Hitosugi T, Nakao S, Hasegawa T, Li Bassi A. Vibrational–electrical properties relationship in donor-doped TiO2 by Raman spectroscopy. J Phys Chem 2016;120:18878–86.
[44] Pascariu P, Homocianu M, Vacareanu L, Asandulesa M. Multi-Functional materials based on Cu-Doped TiO2 ceramic fibers with enhanced pseudocapacitive performances and their dielectric characteristics. Polymers 2022;14:4739.
[45] Prajapat K, Mahajan U, Dhonde M, Sahu K, Shirage PM. Synthesis and characterization of TiO2 nanoparticles: unraveling the influence of copper doping on structural, surface morphology, and optical properties. Chem Phys Impact 2024; 8:100607.
[46] Zhang H, Wang M, Xu F. Generating oxygen vacancies in Cu2+-doped TiO2 hollow spheres for enhanced photocatalytic activity and antimicrobial activity. J.MN. Letters Micro & Nano Lett 2020;15:535–9.
[47] Raguram T, Rajni K. Synthesis and analysing the structural, optical, morphological, photocatalytic and magnetic properties of TiO2 and doped (Ni and Cu) TiO2 nanoparticles by sol–gel technique. Appl Phys A 2019;125:288.
[48] Choudhury B, Dey M, Choudhury A. Defect generation, d-d transition, and band gap reduction in Cu-doped TiO2 nanoparticles. Int Nano Lett 2013;3:25.
[49] Teodoro V, Longo E, Zaghete MA, Perazolli LAJEQ. Influence of Cu-doped TiO2 on its structural and photocatalytic properties. Ecletica Quim 2022;47:130–40.
[50] Radhakrishnan A, Tharmaraj M, Ramani A, Srinivasan NJE. Facile fabrication of CuO modified TiO2 heterostructure for enhanced photocathodic corrosion protection of 304 stainless steel, vol. 6; 2025. p. 21.
[51] Morante N, Tammaro O, Monzillo K, Sannino D, Battiato A, Vittone E, Castellino M, Esposito S, Vaiano VJC. Unraveling the role of CuO in CuxO/TiO2 photocatalyst for the direct propylene epoxidation with O2 in a fluidized bed reactor. ChemSusChem 2025;18:e202401546.
[52] Henderson Michael A. A surface science perspective on TiO2 photocatalysis. Surf Sci Rep 2011;66(6–7):185–297.
[53] Wei Tingcha, Lau Woon Ming, An Xiaoqiang, Yu Xuelian. Interfacial charge transfer in MoS2/TiO2 heterostructured photocatalysts: the impact of crystal facets and defects. Molecules 2019;24(9):1769. https://doi.org/10.3390/molecules24091769. https://www.mdpi.com/1420-3049/24/9/1769. [Accessed 7 May 2019].
[54] Huang Lei, Peng Feng, Ohuchi Fumio S. "In situ" XPS study of band structures at Cu2O/TiO2 heterojunctions interface. Surf Sci 2009;603(17):2825–34. https://doi.org/10.1016/j.susc.2009.07.030. https://linkinghub.elsevier.com/retrieve/pii/S0039602809005111.
[55] González-Burciaga LA, Núñez-Núñez CM, Morones-Esquivel MM, Avila-Santos M, Lemus-Santana A, Proal-Nájera JB. Characterization and comparative performance of TiO2 photocatalysts on 6-Mercaptopurine degradation by solar heterogeneous photocatalysis. Catalysts 2020;10:118.
[56] Zhang Y, Xu X. Machine learning band gaps of Doped-TiO2 photocatalysts from structural and morphological parameters. ACS Omega 2020;5:15344–52.
[57] Samsudin EM, Abd Hamid SB. Effect of band gap engineering in anionic-doped TiO2 photocatalyst. Appl Surf Sci 2017;391:326–36.
[58] Colón G, Maicu M, Hidalgo MC, Navío JA. Cu-doped TiO2 systems with improved photocatalytic activity. Appl Catal B Environ 2006;67:41–51.
[59] Li G, Huang J, Chen J, Deng Z, Huang Q, Liu Z, Guo W, Cao R. Highly active photocatalyst of Cu2O/TiO2 octahedron for hydrogen generation. ACS Omega 2019;4:3392–7.
[60] Khalid NR, Ahmed E, Hong Z, Ahmad M, Zhang Y, Khalid S. Cu-doped TiO2 nanoparticles/graphene composites for efficient visible-light photocatalysis. Ceram Int 2013;39:7107–13.
[61] Rather RA, Singh S, Pal B. A Cu+1/Cu0-TiO2 mesoporous nanocomposite exhibits improved H2 production from H2O under direct solar irradiation. J Catal 2017; 346:1–9.
[62] Balık M, Bulut V, Erdogan IY. Optical, structural and phase transition properties of Cu2O, CuO and Cu2O/CuO: their photoelectrochemical sensor applications. Int J Hydrogen Energy 2019;44:18744–55.
[63] Zhang H, Xu Y, Ouyang X, Ni Y. J.J.o.S.-G.S. Technology, Interplay of dopants and defects in magnetic evolution of La and Fe co-doped TiO 2 nanoparticle, vol. 83; 2017. p. 365–74.
[64] Choudhury B, Dey M, Choudhury AJAN. Shallow and deep trap emission and luminescence quenching of TiO2 nanoparticles on Cu doping, vol. 4; 2014. p. 499–506.
[65] Muscatello A, Iervolino G, Vaiano V, Esposito S. High-performance ceria via supramolecular metal-organic gel precursors for visible-light-driven hydrogen evolution from aqueous glucose. Chem Commun 2025;61:15830–3.
[66] Nick Serpone, Is the band gap of pristine TiO2 narrowed by Anion- and cation-doping of titanium dioxide in second-generation photocatalysts? J Phys Chem B Vol 110/Issue 48.
[67] Thommes M, Kaneko K, Neimark AV, Olivier JP, Rodriguez-Reinoso F, Rouquerol J, Sing KSJP, chemistry a. Physisorption of gases, with special reference to the evaluation of surface area and pore size distribution. IUPAC Technical Report) 2015;87:1051–69.
[68] Karam L, Reboul J, Casale S, Massiani P, El Hassan N. Porous nickel-alumina derived from metal-organic framework (MIL-53): a new approach to achieve active and stable catalysts in methane dry reforming. ChemCatChem 2020;12:373–85.
[69] Ansari F, Sheibani S, Fernandez-García M. Surface modification of Cu2O-CuO photocatalyst on Cu wire through decorating with TiO2 nanoparticles for enhanced visible light photocatalytic activity. J Alloys Compd 2022;919:165864.
[70] Kim HR, Razzaq A, Grimes CA, In S-I. Heterojunction p-n-p Cu2O/S-TiO2/CuO: synthesis and application to photocatalytic conversion of CO2 to methane. J CO2 Util 2017;20:91–6.
[71] Li L, Li W, Yang J, Mao L. Investigation of visible-light absorption in Cu2O/TiO2 heterojunctions with an interstitial at the interface. Phys Status Solidi B 2017;254: 1600420.
[72] Gnanasekaran L, Pachaiappan R, Kumar PS, Hoang TKA, Rajendran S, Durgalakshmi D, Soto-Moscoso M, Cornejo-Ponce L, Gracia F. Visible light driven exotic p (CuO) - n (TiO2) heterojunction for the photodegradation of 4-chloro-phenol and antibacterial activity. Environ Pollut 2021;287:117304.
[73] Chen H, Zhang X, Shen C, Wang Y, Li Z, Cao B, Wang S. Non-thermal plasma degradation of dye wastewater assisted by reverse osmosis process through interfacial mass transfer enhancement. Chem Eng Sci 2023;282:119221.
[74] Chen X, Liu L, Yu PY, Mao SSJS. Increasing solar absorption for photocatalysis with black hydrogenated titanium dioxide nanocrystals. Science 2011;331:746–50.
[75] Liu H, Yang W, Ma Y, Yao J. Extended visible light response of binary TiO2-Ti2O3 photocatalyst prepared by a photo-assisted sol–gel method. Appl Catal Gen 2006; 299:218–23.
[76] Iervolino G, Vaiano V, Murcia JJ, Lara AE, Hernández JS, Rojas H, Navío JA, Hidalgo MC. Photocatalytic production of hydrogen and methane from glycerol reforming over Pt/TiO2–Nb2O5. Int J Hydrogen Energy 2021;46:38678–91.
[77] Wang W, Li B, Yang H-J, Liu Y, Gurusamy L, Karuppasamy L, Wu JJ. Photocatalytic hydrogen evolution from water splitting using Core-Shell structured Cu/ZnS/COF composites. Nanomaterials 2021;11:3380.
[78] Lee G-J, Hou Y-H, Chen C-Y, Tsay C-Y, Chang Y-C, Chen J-H, Horng T-L, Anandan S, Wu JJ. Enhanced performance for photocatalytic hydrogen evolution using MoS2/graphene hybrids. Int J Hydrogen Energy 2021;46:5938–48.

[79] Daugulis AJ, Tomei MC, Guieysse B. Overcoming substrate inhibition during biological treatment of monoaromatics: recent advances in bioprocess design. Appl Microbiol Biotechnol 2011;90:1589–608.
[80] Andrews JF. A mathematical model for the continuous culture of microorganisms utilizing inhibitory substrates. Biotechnol Bioeng 1968;10:707–23.
[81] Suhag MH, Tateishi I, Furukawa M, Katsumata H, Khatun A, Kaneco S. Photocatalytic biohydrogen production using ZnO from aqueous glycerol solution with aid of simultaneous Cu deposition. J Composite Sci 2023;7:361.
[82] Kumaravel V, Imam MD, Badreldin A, Chava RK, Do JY, Kang M, Abdel-Wahab A. Photocatalytic hydrogen production: role of sacrificial reagents on the activity of oxide, carbon, and sulfide catalysts. Catalysts 2019;9:276.
[83] Davis KA, Yoo S, Shuler EW, Sherman BD, Lee S, Leem G. Photocatalytic hydrogen evolution from biomass conversion. Nano Converg 2021;8:6.
[84] Awatani T, Dobson KD, McQuillan AJ, Ohtani B, Uosaki K. In situ infrared spectroscopic studies of adsorption of lactic acid and related compounds on the TiO2 and CdS semiconductor photocatalyst surfaces from aqueous solutions. Chem Lett 2003;27:849–50.
[85] Wang L, Zhang Q, Chen B, Bu Y, Chen Y, Ma J, Rosario-Ortiz FL, Zhu R. Some issues limiting photo(cata)lysis application in water pollutant control: a critical review from chemistry perspectives. Water Res 2020;174:115605.
[86] Baumberger JP, Jürgensen J, Bardwell KJ. The coupled redox potential of the lactate-enzyme-pyruvate system. J Gen Physiol 1933;16:961.
[87] Alberty RA. Calculating apparent equilibrium constants of enzyme-catalyzed reactions at pH 7. Biochem Educ 2000;28:12–7.
[88] Zong X, Yan H, Wu G, Ma G, Wen F, Wang L, Li C. Enhancement of photocatalytic H2 evolution on CdS by loading MoS2 as cocatalyst under visible light irradiation. J.J.o.t.A.C.S J Am Chem Soc 2008;130:7176–7.
[89] Zhang W, Wang Y, Wang Z, Zhong Z, Xu R. Highly efficient and noble metal-free NiS/CdS photocatalysts for H 2 evolution from lactic acid sacrificial solution under visible light. J.C.C. Chem Commun 2010;46:7631–3.
[90] Li Y, Kuang L, Xiao D, Badireddy AR, Hu M, Zhuang S, Wang X, Lee ES, Marhaba T, Zhang W. Hydrogen production from organic fatty acids using carbon-doped TiO2 nanoparticles under visible light irradiation. Int J Hydrogen Energy 2018;43:4335–46.
[91] Cai W, Liu J, Luo Y, Liao Z, Li B, Xiang X, Fang Y. Bifunctional CdS-MoO2 catalysts for selective oxidation of lactic acid coupled with photocatalytic H2 production. J Colloid Interface Sci 2024;675:836–47.
[92] Jiang X, Fuji MJCL. In-situ preparation of black TiO2/Cu2O/Cu composites as an efficient photocatalyst for degradation pollutants and hydrogen production. Catal Lett 2022;152:3272–83.
[93] Muscetta M, Clarizia L, Race M, Andreozzi R, Marotta R, Di Somma I. Visible—Light driven systems: effect of the parameters affecting hydrogen production through photoreforming of organics in presence of Cu2O/TiO2 nanocomposite photocatalyst. Appl Sci 2023;13:2337.
[94] Xiao B, Shen C, Luo Z, Li D, Kuang X, Wang D, Zi B, Yan R, Lv T, Zhou T, Zhang J, Liu Q. Cu surface doped TiO2: constructing Cu single-atoms active sites and broadening the photo-response range for efficient photocatalytic hydrogen production. Chem Eng J 2023;468:143650.
[95] Zhang P, Song T, Wang T, Zeng H. Enhancement of hydrogen production of a Cu–TiO 2 nanocomposite photocatalyst combined with broad spectrum absorption sensitizer Erythrosin B. RSC Advences 2017;7:17873–81.
[96] Lewandowski Ł, Gajewicz-Skretna A, Klimczuk T, Trykowski G, Nikiforow K, Lisowski W, Gołąbiewska A, Zaleska-Medynska A. Towards computer-aided graphene covered TiO2-Cu/(CuxOy) composite design for the purpose of photoinduced hydrogen evolution. Catalysts 2021;11:698.
[97] Wang L, Lei D, Lv Y, Guo R, Wu Y, Wang Z. Experimental study on preparing Cu/TiO2 photothermal catalysts using photodeposition one-step method and its application in catalytic hydrogen production from glycerol. Sustain Energy Technol Assessments 2025;73:104144.
[98] Obregón S, Lee SW, Rodríguez-González V. Loading effects of silver nanoparticles on hydrogen photoproduction using a Cu-TiO2 photocatalyst. Mater Lett 2016;173:174–7.